Additive Manufacturing 85 (2024) 104180

Contents lists available at ScienceDirect

Additive Manufacturing

journal homepage: www.elsevier.com/locate/addma

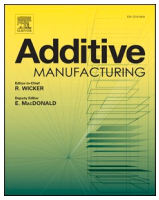

Effect of laser focal point position on porosity and melt pool geometry in laser powder bed fusion additive manufacturing

Joni Reijonen [a,b,*], Alejandro Revuelta [a], Sini Metsä-Kortelainen [a], Antti Salminen [b]

[a] VTT Technical Research Centre of Finland Ltd., Advanced Manufacturing Technologies, Espoo FI-02044, Finland
[b] University of Turku, Department of Mechanical and Materials Engineering, Turku FI-20014, Finland

ARTICLE INFO

Keywords:
Focal point position
Laser powder bed fusion
Melt pool monitoring
Melt pool geometry
Porosity

ABSTRACT

In laser powder bed fusion (PBF-LB) additive manufacturing (AM), the laser beam is the fundamental tool used to selectively melt metal powder layer-upon-layer to form a 3-dimensional part. Studies on the effect of the laser scanning parameters (power, speed, hatch distance, and scanning strategy in general) on part quality are abundant; however, far less emphasis has been given to the effect of the laser beam and how it is focused on the laser-material interaction plane. Here, we have studied the effect of laser beam focal point position on porosity and melt pool geometry in PBF-LB AM. In addition, we also study how the various energy density parameters developed for laser melting processes correlate with melt pool dimensions in a situation where the laser beam focal point position (and the beam diameter and laser intensity change at work plane caused by it), is taken into consideration. Furthermore, we assess the possibility of using co-axial, photodiode-based melt pool monitoring signals as a means to monitor the thermal emissions of the process, and how it correlates with the resulting melt pool geometry. It was found that melt pool penetration experiences a major decrease when the focal point position is shifted by more than ±1 mm (or 30% of Rayleigh length), which could be considered as a tolerance limit for acceptable focus shift in PBF-LB machines. Focus shifts larger than this were effectively captured by the photodiode signals, indicating the potential of using such photodiode-based melt pool monitoring systems for continuous monitoring of focus shift in PBF-LB AM. Finally, it was shown that all the studied energy density parameters, except volumetric energy density, were able to capture the trend in normalized melt pool dimensions when focus position is introduced as a variable. A new energy density metric by normalizing the melt pool monitoring signal intensity with the beam area was introduced and shown to correlate with the normalized melt pool dimensions.

1. Introduction

In laser powder bed fusion (PBF-LB) additive manufacturing (AM), the laser beam is the fundamental tool used to selectively melt metal powder layer-upon-layer to form a 3-dimensional part. Studies on the effect of the main laser scanning parameters, namely laser power, scanning speed, hatch distance, and scanning strategy in general on resulting melt pool geometry, microstructure, and part properties for various alloys are abundant [1–7]. The significant impact of the build chamber environment, namely the type and pressure of the used shielding gas [8] and it's flow velocity over the build plate [9] on the melt pool geometry in PBF-LB has also been established. In addition, various simplified energy density parameters, such as volumetric energy density [10], power density [11], energy density [12], and normalized enthalpy [13], have been developed and used over the years in an attempt to reduce the individual laser processing parameters into one universal parameter that could be used to predict the resulting melt pool geometry. Although some of the energy density parameters consider an ideal Gaussian beam diameter as part of the metric calculation, far less emphasis has been given to the effect of the laser beam and how it is focused on the laser beam-material interaction plane in comparison to the other parameters. Wavelength, beam quality, shape, size, and intensity distribution at focus are key characteristics of a focused laser beam and are determined by the PBF-LB machine architecture, namely by the laser source and all the optics between it and the processing plane.

The beam diameter is known to have a significant impact on melt pool dimensions and the processing conditions in general. Sow et al.

* Corresponding author at: VTT Technical Research Centre of Finland Ltd., Advanced Manufacturing Technologies, Espoo FI-02044, Finland.
E-mail address: joni.reijonen@vtt.fi (J. Reijonen).

https://doi.org/10.1016/j.addma.2024.104180
Received 10 January 2024; Received in revised form 30 April 2024; Accepted 1 May 2024
Available online 6 May 2024

[14] compared the use of a typical 80 μm laser spot diameter with Gaussian intensity distribution used in PBF-LB to a large 500 μm spot with top-hat intensity distribution. The larger spot size enabled increased hatch distance, increasing productivity, and the top hat intensity distribution also suppressed vaporization, resulting in shallow and wide melt pools and reducing spatters and porosity. The drawback was an increased tendency for thermal distortion on the macroscopic level due to an overall increased heat input to the part.

Another important aspect of a focused laser beam is the focal point position in relation to the work plane and its stability over time. Focus shift due to thermal lensing in the optical components in PBF-LB is a known phenomenon [15] and something that needs to be checked and corrected on PBF-LB systems periodically, usually done alongside the 6- or 12-month interval maintenances of the machines. Dirt on and degradation of the optical components are the main reasons for focus shift in the process over time. For laser cutting, it has been shown that focus shift due to thermal lensing can be severe enough to compromise cut edge quality [16]. However, there have been no conclusive studies on establishing how a large focus shift is acceptable before part quality is significantly impaired in PBF-LB AM. Furthermore, it would be beneficial to continuously monitor the melting conditions and to determine from the monitoring signals if the process has remained stable and the focus position within acceptable tolerances.

Patel et al. [17] studied the effect of focus positions above the laser-material interaction plane in PBF-LB for AlSi10Mg to produce large beam diameters at the surface. This resulted in wider, shallower melt pools and suppressed keyhole porosity formation, reaching densities > 99.98%. Bean et al. [18] studied the effect of laser focus position in PBF-LB on porosity, surface roughness, and the tensile properties of Inconel 718. They varied focal point position between −5 mm and +5 mm compared to powder bed surface and noted effects on all properties as a function of focus position. In their study, the measured as-built porosities of ~1% even for the best condition were all together very high for PBF-LB and no melt pool geometry measurements were conducted. Paraschiv et al. [19] studied the effect of focal point position in PBF-LB of Inconel 625 and noted the effects on melt pool geometry of single-tracks, but small-to-no effect on part-level porosity and tensile properties. The focal point position was varied within a very small range of ±0.5 mm, which was most likely well within the depth of focus (not reported) of the used laser beam and hence the small impact. On the contrary, Metelkova et al. [20] studied the effect of focus position on melt pool geometry in PBF-LB of 316 L stainless steel, but with very large focal point positions of ±6 and ±8 mm. They concluded a much more severe impact of focus position on penetration than the width of the melt pool, especially with small energy inputs, where the impact on bead width was negligible. Furthermore, the differences between using a divergent or convergent beam on melt geometry were highlighted. In previous studies, the extremes have been explored, but no attempt has been made to establish a practical range within which the focus position can vary without severe impact on melt pool geometry and part properties in PBF-LB AM. During normal operation between the yearly maintenance intervals of a commercial PBF-LB machine, we have experienced, at maximum, a focus shift of up to ~2.0 mm in the focus position. Usually it has remained within the range of 0.5−1.5 mm, as identified by measuring the beam diameter over the caustic to identify focal point position in relation to the work plane. Therefore, it is necessary to study the effect of and establish limits for an acceptable shift in focal point position before part quality is impaired.

In this work, the effect of laser focus position within a range of ±5 mm on porosity and melt pool geometry of 316 L stainless steel in PBF-LB AM is established. In addition, we have evaluated how the various simplified energy density parameters developed for the laser melting processes correlate with melt pool dimensions in a situation where the laser focus position, and the beam diameter and laser intensity change at the work plane caused by it, is taken into consideration. Furthermore, we assess the possibility of using co-axial photodiode-based melt pool monitoring signals as a means to monitor the total energy density of the process, and how it correlates with the change in focus position and the resulting melt pool geometry.

2. Materials and methods

SLM 125 HL, from SLM Solutions GmbH, was used for the PBF-LB experiments. The laser source was IPG YLR-400-SM fiber laser emitting at 1070 nm central wavelength and having a maximum power of 400 W. The Scanlab Intelliscan 25 galvanometer scanner is used for xy-positioning of the laser beam, and the laser focus, i.e., the z-distance is adjusted programmatically with the Scanlab Varioscan 40 dynamic focusing unit. Laser focus at the work plane is defined as 0 mm. A negative change in the focus setting means a decrease in the focal length, hence the focus moves above the work plane. A positive change is then an increase in the focal length, hence the focus is below the work plane. This is illustrated in Fig. 1. It is good to notice, that with this type of focus position adjustment setup, the focal length is not constant, which also has an impact on the resulting spot size when the focus position is varied. Laser beam characteristics over the beam caustic at the studied intervals (−5.0, −3.0, −2.0, −1.0, −0.5, 0.0, +0.5, +1.0, +2.0, +3.0, +5.0) mm was measured using a focus beam profiler FBP-1KF-5.3–3x, together with the RayCi Pro version 2.7.8 software from CINOGY Technologies GmbH. Background calibration was performed prior making the measurements. The device was water cooled, and the sensor temperature was between 27.4−29.0°C during the measurements. For determining beam diameter, the accuracy is reported as 2−4% by the equipment manufacturer, based on which a conservative 4% error was assumed in the results presented in this paper.

An experimental build job was designed to study the effect of the laser focus position on melt pool geometry, part porosity, and melt pool monitoring signal. The build layout is shown in Fig. 2. Argon with purity of ≥ 99.999% was used as the shielding gas. The flow speed was set to 7.0 m/s, as measured in the 40 mm inner diameter inlet pipe, corresponding to ~528 l/min volumetric flow. As it is known that the shielding gas flow conditions vary based on the location on the build area, the specimens were grouped around the central area of the platform on a compact footprint and not too far away from one another in the study group. Furthermore, we have previously measured the impact of location on shielding gas flow speed on the very same SLM 125 HL machine and have found out that the variation in gas flow speed above the entire build plate is quite small, as the build area is small (only 125×125 mm) [9]. The location-depended effects due to shielding gas flow become much more evident in PBF-LB machines having larger build areas, as shown for the machine used by Yang et al. [21] where the build area was 450×450 mm.

The specimens were built directly onto a 316 L stainless steel platform without any support structures. The platform pre-heat temperature was set to 30°C. Gas atomized 316 L powder with a particle size distribution of D_{10} = 19.4 μm D_{50} = 30.5 μm D_{90} = 47.7 μm from Carpenter Additive was used. The layer thickness was 30 μm, the linear re-coating speed was ~217 mm/s, and a soft polymer composite re-coater blade with a round profile was used for powder spreading. The specimens were separated from the platform with electric discharge machining. No post-process heat-treatment was applied, and the specimens were used for further analyses in the as-built condition.

Specimens 1−11 were made by varying the focus position, while keeping the other laser parameters constant. Specimens 12−17 were made with a constant focal point position −3 mm, while varying the laser beam scanning speed, power, and hatch distance to produce various energy densities. The laser parameters for each specimen are listed in Table 1. The nominal reference (specimen 6) was produced with standard 316 L parameters developed for the 30 μm layer thickness process. The scanning strategy called Stripes was used for all specimens. It consisted of bi-directional hatching vectors with a stripe length set to 10 mm. The scanning orientation was varied between layers as listed in

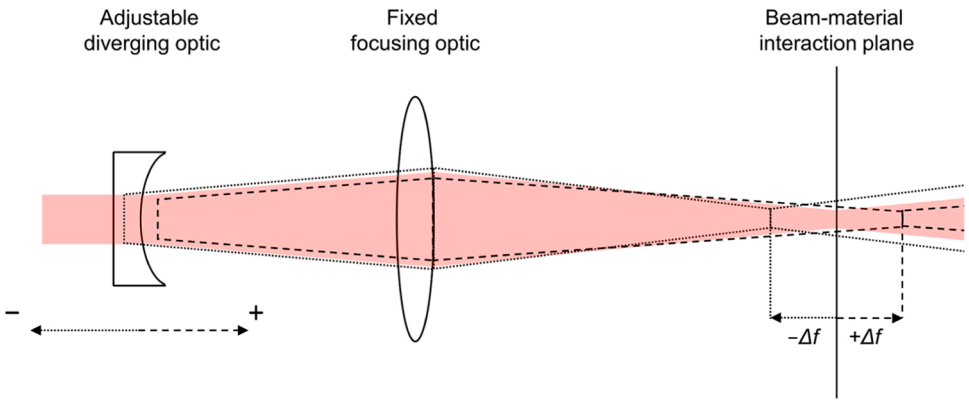

Fig. 1. Schematic illustration of the focal point position adjustment with the system used in the experiments. Transparent red illustrates 0 mm setting, dashed line a positive change and dotted line a negative change in focal point position.

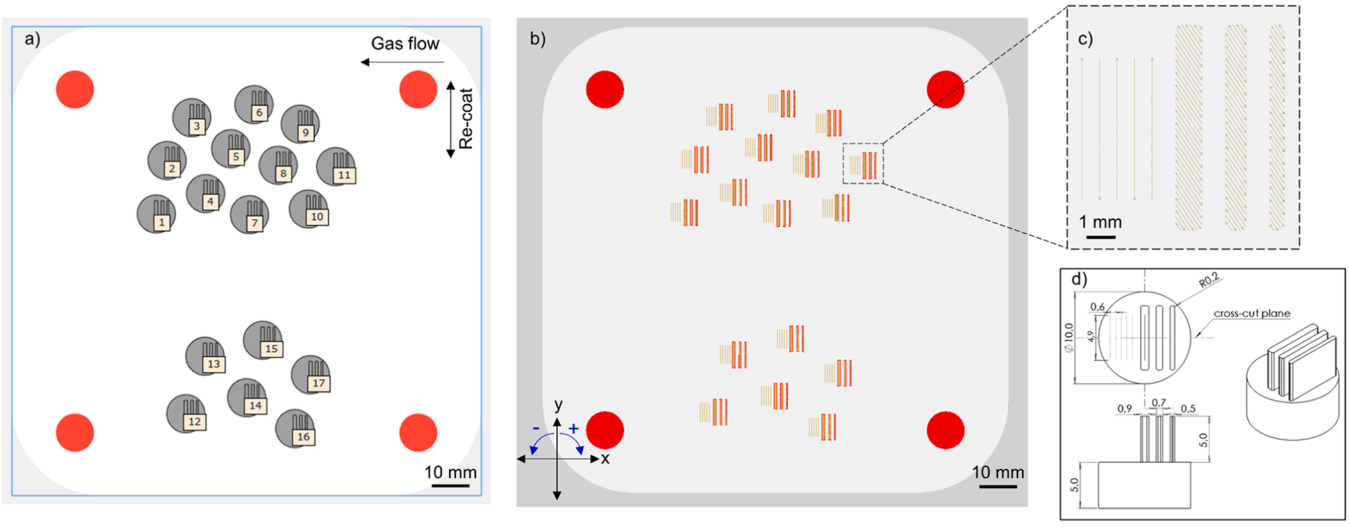

Fig. 2. (a) layout of the specimens in the building platform, (b) layer number 168 of the build, showing the placement of the single tracks, (c) detailed view of the single tracks and scanning strategy, and (d) specimen dimensions.

Table 1
Process parameters for the specimens used in the experiments.

No.	Focus [mm]	Beam diam. [mm]	Power [W]	Speed [mm/s]	Hatch [mm]	VED [J/mm^3]	Power density [W/mm^2]	Energy density [J/mm^2]	ΔH/h_s	Purpose
1	−5.0	0.138	200	800	0.12	69.4	13333	16.7	4.0	Negative focus position
2	−3.0	0.100	200	800	0.12	69.4	25562	32.0	6.2	Negative focus position
3	−2.0	0.085	200	800	0.12	69.4	35072	43.8	8.1	Negative focus position
4	−1.0	0.077	200	800	0.12	69.4	42584	53.2	10.1	Negative focus position
5	−0.5	0.076	200	800	0.12	69.4	43730	54.7	10.3	Negative focus position
6	+0.0	0.078	200	800	0.12	69.4	42310	52.9	10.5	Nominal ref.
7	+0.5	0.078	200	800	0.12	69.4	42353	52.9	10.3	Positive focus position
8	+1.0	0.085	200	800	0.12	69.4	35622	44.5	10.1	Positive focus position
9	+2.0	0.097	200	800	0.12	69.4	27070	33.8	8.1	Positive focus position
10	+3.0	0.116	200	800	0.12	69.4	18957	23.7	6.2	Positive focus position
11	+5.0	0.156	200	800	0.12	69.4	10437	13.0	4.0	Positive focus position
12	−3.0	0.100	150	600	0.12	69.4	19171	32.0	5.4	same VED as ref.
13	−3.0	0.100	250	1000	0.12	69.4	31952	32.0	7.0	same VED as ref.
14	−3.0	0.100	250	800	0.15	69.4	31952	39.9	7.8	same VED as ref.
15	−3.0	0.100	400	800	0.12	138.9	51124	63.9	12.4	same PD, same ED as ref.
16	−3.0	0.100	400	1000	0.12	111.1	51124	51.1	11.1	same PD as ref.
17	−3.0	0.100	400	800	0.15	111.1	51124	63.9	12.4	same PD and ED as ref., high hatch

Appendix A. Contour or border vectors were not used. The hatch distances for each specimen are reported in Table 1. Various energy density parameters have been developed over the years for laser welding and PBF-LB in an attempt to reduce the individual input parameters to a single parameter that could be used to predict the output melt geometry. We have defined the parameters as follows. Volumetric energy density is

defined as $VED = P/vhLT$ [10], where P = laser power, v = scanning speed, h = hatch distance, and LT = layer thickness. Power density as $PD = P/\pi a^2$ [11], where a = beam radius at work plane and energy density is defined as $ED = PD/v$ [12]. Normalized enthalpy $\Delta H/h_s$ is defined as described in [13]. In this study, we assess how these energy density parameters work in predicting the melt pool dimensions (width and penetration) in a situation where the laser focus position (and the beam diameter and laser intensity change at the work plane caused by it), is taken into consideration. *VED* does not include any term characterizing the beam size in the equation, while *PD*, *ED*, and $\Delta H/hs$ include the beam area as πa^2. Furthermore, a preliminary investigation is conducted on the possibility of using the melt pool monitoring signal as a similar metric to monitor the total energy density of the process and how it correlates with the resulting melt pool geometry.

X-ray computed tomography (xCT) was conducted on the manufactured specimens with GE Phoenix v|tome|x s system. The output data was an 8-bit image stack, having a voxel resolution of 7.5 μm. Processing and analysis of the xCT-data was conducted using ImageJ software (version 1.54 f). The xCT-data was denoised using the Non-Local Means Denoising algorithm [22], available as a plugin for ImageJ, with the auto estimate sigma setting enabled and smoothing factor set to 2. The 8-bit (grayscale values between 0−255) image stack was binarized to solid material (white) and defects (black). The threshold for binarization was selected manually, as none of the automatic threshold selection algorithms implemented in ImageJ provided acceptable segmentation of the defects from the solid for the xCT data used. The defect data (volume and centroid location of each identified defect) was then segmented and extracted by using the 3D objects counter function, introduced in [23] and available as a plugin in ImageJ. Similarly, an inverse segmentation based on a selected threshold was made to extract the part from the background to get the total volume of the part for calculating the total porosity. By testing with slightly different threshold selections, the error in determining total porosity with this method was estimated as 5% of the measured value or 0.002 percentage points in the total porosity, whichever is greater.

Metallographic cross-sections were prepared by cutting the samples from the plane shown in Fig. 2(d) and then polishing to mirror finish. The ZEISS Axio Observer Inverted Microscope was used for microscopy analysis. Panorama images with 5x magnification were acquired to cover the whole cross-sectional area in the polished state for optical porosity measurements. The porosity was measured from one cross-section of each sample. The cross-section was made from the middle of the specimens, along the build direction. This equals porosity analysis areas of 5×10 mm^2 for the cylinder, and 5×0.9 mm^2, 5×0.7 mm^2 and 5×0.5 mm^2 for the thin walls, respectively. Porosity was measured from the panorama images using the Particle Analyzer function in ImageJ software (version 1.54 f). Thresholding was done in a similar manner as for the xCT data, and the same measurement error was assumed. After this, the polished cross-sections were further etched with Aqua Regia to reveal the microstructure and melt pool boundaries. Images from the melt pool cross-sections were acquired with 20x magnification. Average width and penetration of the melt pools were then measured from the five single tracks from each specimen. In addition, the average total melt pool height was measured from the top layer of the cylinder, using 14−20 melt pools per specimen for the measurement. An example of the melt pool dimensional measurements is shown in Fig. 4(a). The metric melt pool total height is measured as defined in [24].

PrintRite3D melt pool monitoring system from SigmaLabs Inc. was used for process monitoring. The system is based on the usage of three different photodiode sensors mounted on-axis to the optical path of the laser to monitor the thermal emissions at different wavelengths in the visible and near-infrared spectrum. The three sensors are named as Thermal Energy Density (TED) and Thermal Energy Planck high and low (TEP high and TEP low). The setup is detailed in [25]. A focusing lens with a focal length of 25 mm is placed before the sensor to focus the light to the sensor detector. The field of view of the sensors at the laser-material interaction plane is circular with a diameter of approximately 60 mm. This has been determined following a procedure as defined in [26], by moving a light source at specified x,y locations on the beam-material interaction plane and recording the photodiode signal response with a multimeter. The light source was a 1 mm diameter aperture backlit with a white LED. A Gaussian surface (R^2=0.9837) was fitted to the data, and the edge of the field of view was determined to be at the location where the intensity drops to 5%, as defined also in [26]. Laser on/off signal and the scanner xy-position are stored simultaneously with the photodiode signals at 100 kHz frequency. The data is stored on a layer-by-layer basis to Hierarchical Data Format version 5 (HDF5) files. The build job used in this study consisted of 334 layers, each generating around 10−40 Mb of data depending on the amount of scanning vectors in each layer. The TED sensor is monitoring a wide range of wavelengths, nominally from 450−900 nm, while the TEP sensors have narrow band filters (TEP low 636 ± 5 nm and TEP high 650 ± 5 nm) before them. The actual, measured spectrum received at each photodiode while laser melting stainless steel is provided in Appendix B, in Fig. B.3. Together the TEP ratio could be used as a two-color pyrometer. In this study, the signal intensity captured by the receiving sensor is used as the metric, and no attempt is made to convert signal intensity to absolute temperature.

In this study, the authors have deliberately chosen to use commercially available PBF-LB machine, laser beam profiler and melt pool monitoring unit along with the photodiodes and associated filters as provided by the system manufacturer. This was done in order to maintain practical relevance of the study and provide useful information also to the practitioners of PBF-LB, who could be using same equipment.

3. Results and discussion

3.1. Laser beam characterization

The laser beam propagation over the caustic was analyzed using RayCi Pro software, first with three power levels (60 W, 100 W, and 400 W) to calculate the beam quality factor (M^2 = 1.36−1.47), Rayleigh length (z_R = 2.84−3.11 mm), and beam waist diameter (d_0 = 72.6−78.5 μm) of the used laser beam and optical configuration over the typical laser power levels used in the system. Then the laser beam cross-sections at the beam-material interaction plane with the studied focus position intervals were further analyzed using the same 200 W laser power as in the manufacturing of the corresponding specimens. The intensity profiles over beam cross-sections at each studied focus setting are shown in Fig. 3(a). From these images, the RayCi Pro software automatically identifies the beam cross-sectional area and diameter in x and y directions (Fig. 3(c)). A slightly elliptic shape, instead of a perfect circle, is used for defining x and y axis orientations and calculating the average beam diameter (Fig. 3(d)) with D4σ criteria as per standard EN ISO 11146–1. The average beam diameter presented in Fig. 3(d) is then the average width of the ellipse, and the error bars corresponds to the ±4% in the diameter, as indicated by the equipment manufacturer for the accuracy of determining the beam diameter. 16 frames were recorded by the measuring device for each spot size measurement, which corresponded to an approximate duration of 1.8 seconds. The images shown in Fig. 3(a) are the output from the measuring software, that is, a time-averaged image from those 16 frames captured during the ~1.8 seconds. In Fig. 3(a), the result is scaled as such that maximum intensity of each spot size measurement is shown as 255 and the sensor was not saturated. The detector sensitivity was not adjusted between measurements, or if it is, it is done automatically by the Focus Beam Profiler equipment. Fig. 3(b) shows the absolute intensities, on a same scale for all the measurements, whereas Fig. 3(a) shows relative intensities, relative in the sense that within that single spot size measurement, the intensities are scaled to 0−255. The images in Fig. 3(a) are the raw output from the measuring device.

Fig. 3(b) further shows an intensity profile over the beam cross-

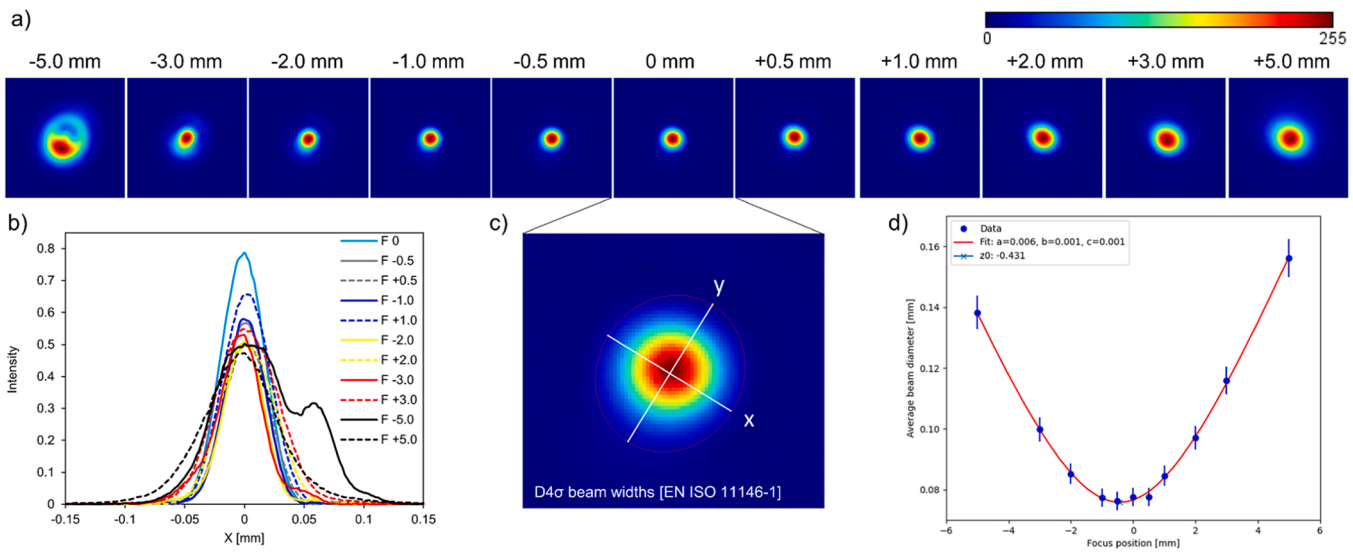

Fig. 3. Laser beam characterization with (a) intensity images of beam cross-sections, (b) intensity profiles over x-axis, (c) example of beam xy-width determination, and d) D4σ average beam diameters calculated as per EN ISO 11146–1.

section along the defined x-axis. As can be seen from Fig. 3(d), the beam diameter is smallest around the focus and increases when beam diameter is measured outside the tightest focus to either direction, as expected. Of the studied focus position intervals, the smallest beam diameter was measured as 76.3 ± 3.1 μm at focus position −0.5 mm. Adding the hyperbolic fit of beam propagation to the data as defined in EN ISO 11146–1, the beam waist location z0 is identified at −0.431 mm.

Between focus positions −1.0 mm and +0.5 mm, the beam diameter remains effectively constant within the 4% measurement accuracy of the system. Beyond this range, the beam diameter starts to increase significantly, reaching 156.2 ± 6.2 μm at position of +5 mm and 138.2 ± 5.5 μm at position of −5 mm, respectively. This difference should not be there for an ideal Gaussian beam propagation, and could be due to the difference in propagation of the beam intensity in the directions, as seen from Fig. 3(a) and (b), where the beam intensity profile in the negative focus position is already far from an ideal Gaussian distribution. It is important to notice, that in real laser processing systems, the beam never behaves like an ideal beam, but with some deviation from it. In addition to the beam diameter, the corresponding change in the intensity distribution, and peak intensity as the focus position changes, is notable. At focus position 0 mm, the peak intensity is 0.79, whereas for the +5 mm focus position the peak intensity is already 40.5% lower at 0.47.

3.2. Melt pool geometry

Fig. 4 shows the results of the measurement of melt pool dimensions as a function of focus position. To characterize the melt pool depth, two separate measurements were used, as shown in Fig. 4(a). First is the penetration defined as how much the melt pool, as measured from the single-scan tracks, penetrates the previous layer. Second is the melt pool total height, measured from the top layer scan tracks in the cylinder specimen. The width is measured only from the single-tracks; as for hatch scanning, the overlap between melt pools prevents reliable measurement of individual melt pool widths. Moreover, the scan vectors are rotated between layers; hence, only the single-tracks are perpendicular to the cross-sectional cut made for the microscopy.

The melt pool depth inversely follows the trend of the beam diameter, as focus position is changed. The melt pool depth is highest when the laser is at focus, or slightly below the laser-material interaction plane. The highest melt pool depth is measured at the focus position +0.5 mm ($d = 168 \pm 8$ μm, $p = 83 \pm 13$ μm). This is in good agreement with earlier studies from laser welding, where usually highest melt pool depths can be achieved when the laser is focused slightly below the laser-material interaction plane [27]. While the focus remains within the range of ±1 mm, the variation in average melt pool penetration is 13% and for melt pool height 8%, which are comparable to the observed intra-specimen variations of 10−23% for penetration and 5−9% for

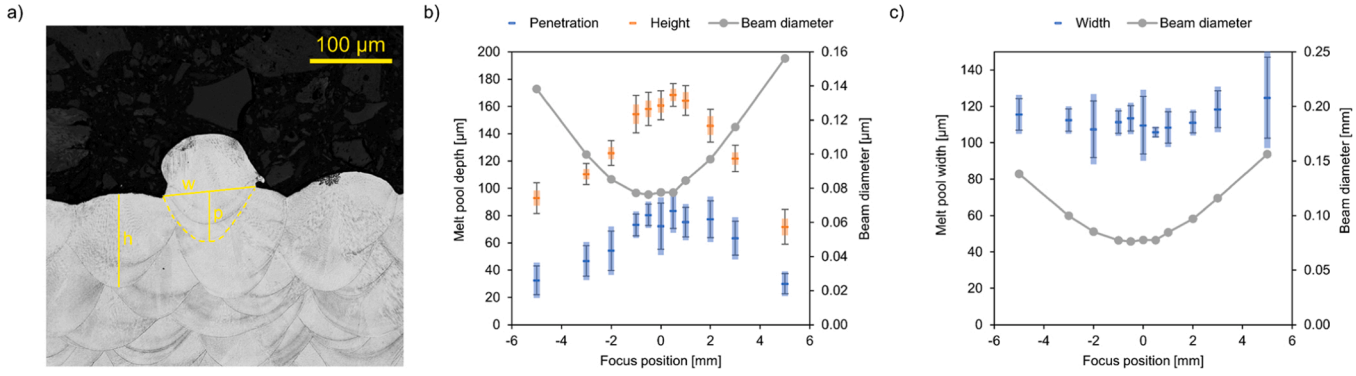

Fig. 4. (a) measurement of melt pool dimensions, (b) resulting penetration *p* and height *h* and (c) width *w*, as a function of laser focus position and beam diameter. In (a−b) for the measured melt pool dimensions, line marks the mean the transparent colored error bar is the 95% confidence interval and the whiskers are the sample standard deviation.

height, at focus positions in range of ± 1 mm. Once shifted more than this to either positive or negative direction, a major decrease in melt pool depth can be observed. The gradient in the decrease is steeper when focus position moves to the positive direction, reaching the lowest melt pool depth (d = 83 ± 13 μm, p = 30 ± 7 μm) at +5 mm. This is a decrease of 50% in depth and 64% in the penetration compared to the +0.5 mm focus position. The effects of the focus position on melt pool width (Fig. 4(c)) are more subtle. It can be seen that, on average, the melt pool widths tend to be smallest close to the focus and increase slightly when moving away from the focus. However, due to the relatively high scatter in the 5 measurements, the 95% confidence interval for calculating the average is quite high and statistically no significant difference exists. The lowest melt pool width is measured at +0.5 mm focus position (w = 106 ± 2 μm) and highest at +5 mm (w = 125 ± 22 μm), a 15% difference. Although the impact of focus position on weld width is much less severe than on melt pool depth, they are in good agreement. At or close to the (±1 mm) focus, narrow and deep melt pools are obtained. When shifted more than this, the beam diameter at the laser-material interaction plane is increased accordingly, which increases the melt pool widths slightly, but result in significant and quite drastic loss of penetration, as the specific laser intensity (J/mm^2) is reduced when the beam size increases, as seen in Fig. 3(b).

3.3. Porosity

The total percentage of porosity measured from xCT data in the specimens as a function of focus position and beam diameter is presented in Fig. 5(a). The total porosities within the cylinders are extremely low at ≤0.004% for all the studied focus positions. For the thin walls, there is, on average, ~10x increase in the total porosity. The reason for this is further elaborated in Section 3.4. Furthermore, from the thin walls, the differences in total porosity between the studied focus positions are more easily distinguished. When the focus is above the work plane between −5 and −0.5 mm, the porosity remains relatively constant. Once at focus and slightly below the work plane from 0 to +2 mm, there is a slight decrease in porosity. Once the focus is placed below the work plane by more than +3 mm the porosity starts to increase. The most significant change in porosity is observed when the focus is at +5 mm below the work plane. In Fig. 5(b), the same relationship is plotted but with total porosity as measured from a single polished cross-section for the cylinders and thin walls as the response. First, it can be noticed that, on average, the absolute porosity values are higher than the respective ones measured from the xCT data. For the cylinders, the difference is most obvious. The porosities measured for these from the polished cross-sections are between 0.01−0.03%, while the corresponding values from xCT data are between 0.001−0.004%. This difference is due to the different resolutions of the methods. The xCT scanning is limited on image resolution by the specimen size, and here a voxel resolution of 7.5 μm was obtained, and a limit of ≥2 voxel indication was imposed for classifying as defect and not noise. For the optical microscopy on the polished cross-sections, an image resolution of 1.45 μm was obtained with 5x magnification panorama images that cover the whole sample cross-section. With such high resolution, even the smallest (<15 μm) residual gas pores are identified, which are omitted by the xCT method. In fact, 97% of the pores identified from all the cylinder cross-sections had an effective diameter smaller than 15 μm, assuming a spherical shape. These correspond to 63% of the total share of porosity in the cross-sectional analysis of the cylinders. Even if numerous, such small and mostly spherical and evenly distributed gas pores have a negligible effect on macroscopic properties, such as tensile strength and fatigue, compared to larger and/or more irregular shaped defects, especially those close to surface [28]. Furthermore, the presence of such residual small, spherical gas porosity in PBF-LB parts is not process-parameter dependent, but rather introduced by the porosity already present in the feedstock powder [29].

Further comparison between the two porosity measurement methods reveals interesting insights. When comparing the total porosity as measured from the cylinders, both methods capture the same trend as a function of the focus position. However, for the thin walls, the same trend is only observable when measured from the xCT data, while the porosities measured from the polished cross-section have much more scatter. This highlights the limitations of the porosity analysis from single cross-sections, as that one cross-sectional sample may or may not be representative of the whole population. With the thin walls, this effect is more pronounced than with the larger cylinder, because the thin walls have a much smaller cross-sectional area represented in the analysis, and hence the presence or absence of even singular defects on that cross-section start to have a significant effect on the measured total porosity. Furthermore, the cross-sectional analysis does not provide comprehensive 3-dimensional spatial information of defect locations within the geometry, which can also reveal interesting phenomena as shown later in Section 3.4. Therefore, in all the subsequent analyses done within this paper, the xCT data is used for deriving porosity-related information.

The defect size distributions shown in Fig. 6(a−b) and defect density, as in the number of defects in a given volume of material shown in Fig. 6 (c), were further analyzed from the xCT data. All voids in the material are labelled as defects and it is believed vast majority of them represent

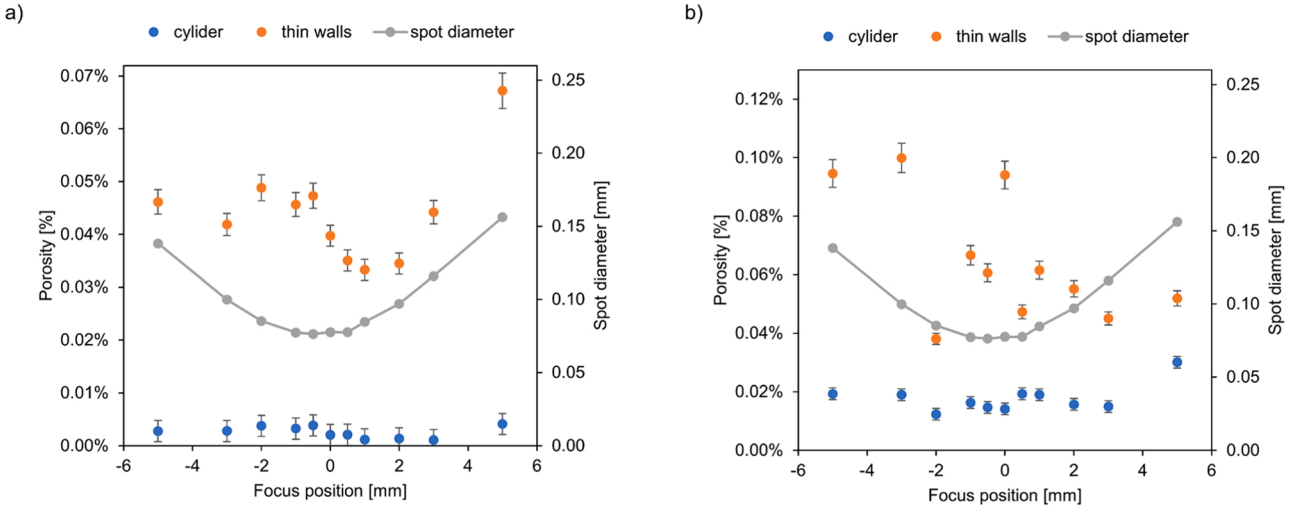

Fig. 5. Total porosity as measured from (a) xCT and (b) OM as a function of focus position and beam diameter.

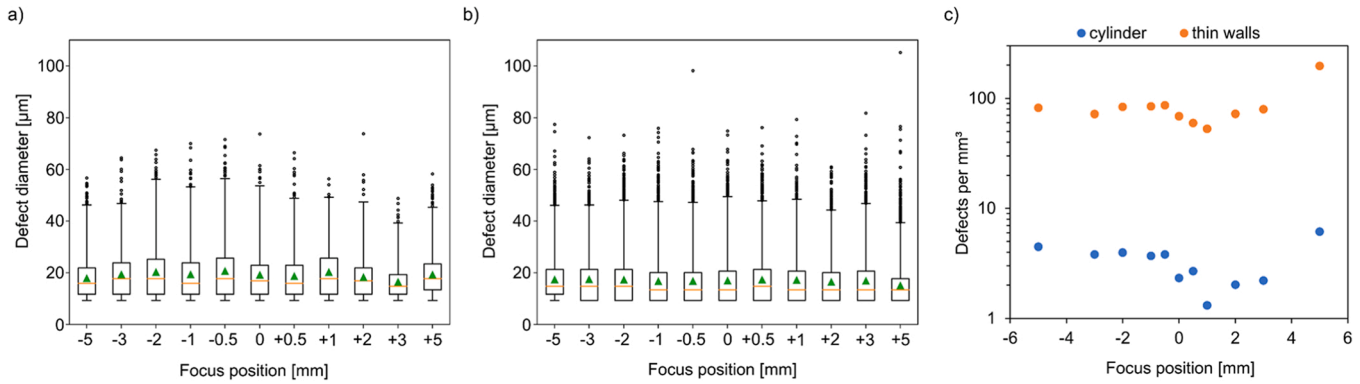

Fig. 6. Boxplots of defect size distributions for (a) cylinder and (b) thin wall sections of the specimens as a function of focus position. Number of defects per volume of material as a function of focus position is further shown in (c). In (a–b) boxplots, the line marks the median, triangle the mean, box the 25th and 75th and the whiskers 1st and 99th percentiles of the data. Outliers are marked with circles. Notice the logarithmic scale of the y-axis in (c).

pores, although if for example cracks would be present, these are also voids and would be classified as defects in the analysis. There is no major difference between the defect size distributions as a function of focus position. In the defect density, shown in Fig. 6(c), we see clear differences as a function of focus position, the trend being similar as with the total porosity measurement of the specimens (see Fig. 5). Therefore, the observed changes in the total porosity as a function of focal point position seems to be mainly due to an increase in the number of defects, not an increase in the size of the defects. The defects are relatively small in size with mean diameter in all specimens between 15–21 µm, and the largest defect (thin walls, focus set to +5) was ~110 µm in diameter. It can be noticed that along with the increase in the number of defects when processing thin walls instead of the cylinder, the occurrence of larger defects above 60 µm in diameter is also increased in the thin walls.

3.4. Porosity formation mechanisms

During the analysis of the xCT data, we noticed that most of the defects, in all the studied specimens and within the cylinder and the thin-walled sections, seemed to be concentrated on the edges close to the surface and much less on the core. To illustrate this, Fig. 7 shows a projection through the xCT data in the build direction with all the defects found in the 3D-volume overlaid to a single 2D-plane. As seen in Fig. 7(c, f), the +5 mm focus condition shows an increased number of defects also on the core and in this regard deviated from the other

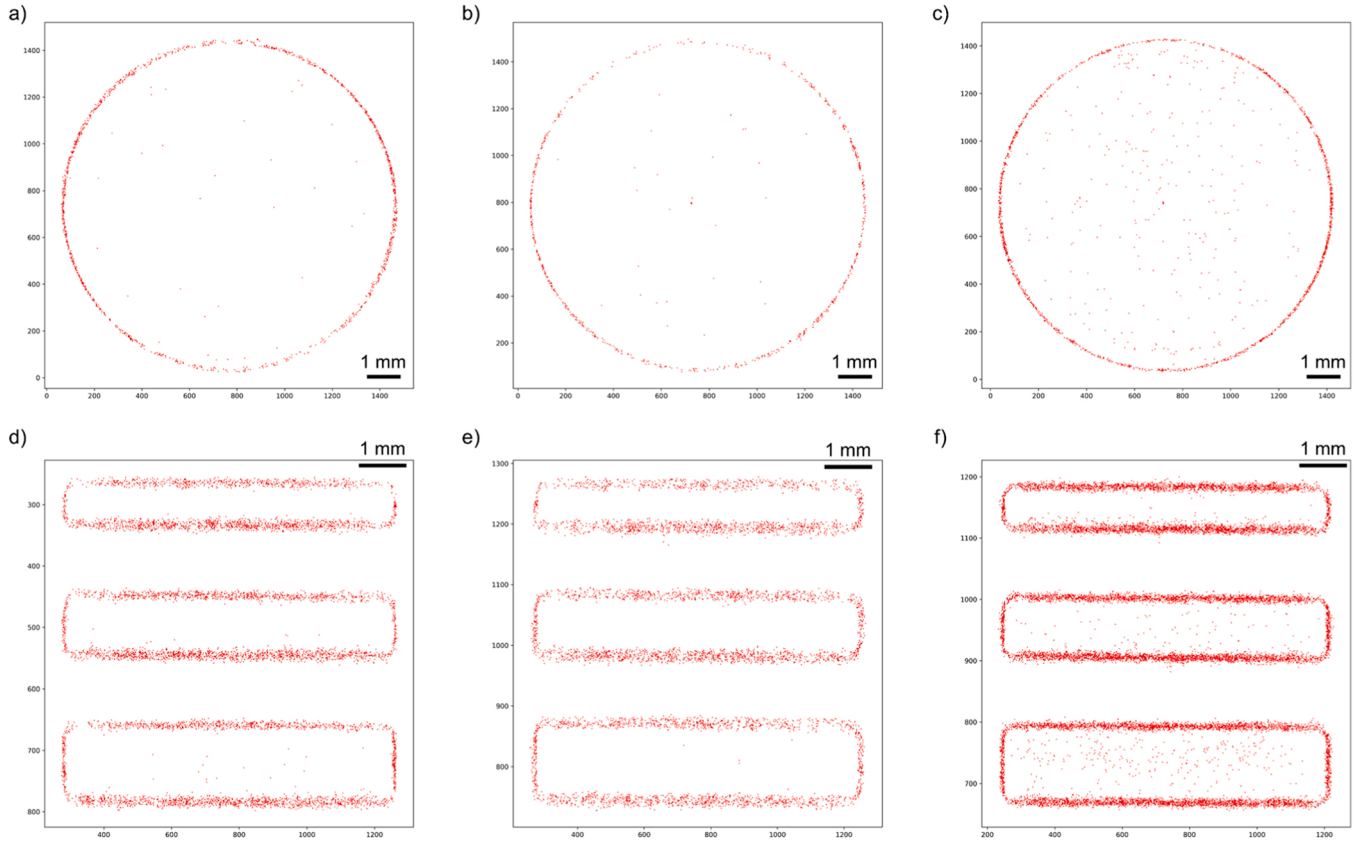

Fig. 7. Defect locations projected from build direction to xy-plane for (a–c) cylinder and (d–f) thin-walled sections of specimens produced with different focus positions: −5 mm (a, d), 0 mm (b, e), and +5 mm (c, f).

specimens. The porosity percentages as calculated separately for the border and core regions (shown in Fig. 8) quantifies the difference. It can be seen, that in the +5 mm condition, significant increase in defects also in the core are seen. In a more detailed analysis (see Fig. 9), these defects were observed to be mainly of non-spherical shape, and having maximum dimensions even larger than those implied in Fig. 6. This is because, for Fig. 6, from the total defect volume that is measured, a spherical defect is assumed for the diameter determination, whereas if the defect is long but narrow, it would have a small total volume, but nevertheless the maximum dimension may be surprisingly large. As seen in Fig. 9(e), the maximum dimension of a defect exceeded 200 μm. Another aspect is that many of these irregularly shaped defects were observed to not be single defects, where all the dark pixels corresponding to a void would be connected in 3D, but rather the defect had solid material in between, essentially separating the defect into multiple smaller ones, even as it could have formed during a single event. In the image analysis conducted, these would be then segmented as multiple smaller defects, instead of a single large one. Due to the non-periodic appearance of these defects in the bulk of the material and the irregular shapes, it is believed that such defects found only in the +5 mm focus condition are caused by a different phenomenon than the defects concentrated on the edges of all the specimens. The presence of these defects would explain why the total porosity seen in Fig. 5 is significantly higher for the +5 mm focus position, compared to all the others. In the +5 mm focus position condition, the measured average melt pool penetration ($p = 30 \pm 7$ μm) and average melt pool height ($d = 103 \pm 36$ μm) were the lowest within the studied range. Based on the criteria defined by Tang et al. [30] for systematic lack of fusion as $L^* \geq LT$, the depth of overlap between adjacent melt pools (L^*) in this condition was measured as 42 ± 9 μm, which is still larger than the nominal 30 μm layer thickness (LT). Five measurements were made for calculating average L^*, of which the smallest was measured at 33 μm, which is already very close of not meeting the criteria. Nevertheless, for such conditions where $L^* \geq LT$ holds, it is further defined in [30] that if $(h/w)^2 + (LT/d)^2 \leq 1$ is not met, lack of fusion porosity would be present. For the measured average melt pool dimensions in +5 mm focus position condition, the equation would give $0.08 \leq 1$, hence lack of fusion should not occur. However, it is believed that due to the dynamic melting conditions and resulting variation in melt pool dimensions, occasionally insufficient penetration to the previous layer, or lack-of-fusion between adjacent hatches may already start to occur within some of the >10000 hatches that constitute the part studied here, causing the stochastic, rather than systematic, lack-of-fusion porosity seen in Fig. 9(b, e).

For the defects concentrated on the part edges, we have identified a different formation mechanism. The scanning strategy (shown in Fig. 2 (b)) used in this study consists of bi-directional laser vectors, having the start and stop points of the vectors always on the part edges. The vector direction alternates between subsequent vectors, hence it is called bi-directional. It was hypothesized, that the defects are formed either at the starts or the stops of the laser vectors. By analyzing the xCT data at the beginnings and endings of the single tracks on the top of the cylinder surface, we observed defect formation at the ends of the laser vectors, not at the beginnings (Fig. 10 (a–b)). The occurrence of such defects was more frequent in the specimens produced with higher laser powers than the nominal 200 W, although the phenomenon was also seen with the nominal 200 W used in the study. Fig. 10 (c–h) shows xCT data of the single-track vector endings, longitudinal to the direction of the laser vector and forming weld. It can be clearly seen in Fig. 10 (c, f, g), that the keyhole, caused by vaporization and vapor depression during the laser melting process, has remained open after solidification. Once the laser is turned off at the end of each scan vector, the heat source is removed almost instantly (laser switch off response time of the used system was ~10 μs), cooling and solidification begins. The solidification rate during PBF-LB is known to be extremely fast at around 0.4–1.0 m/s [31,32], which in this case is also faster than the speed at which the molten metal would flow and fill the keyhole opening, hence leaving behind a very distinctive keyhole-shaped hole after solidification.

As the keyhole, and the surrounding molten metal, movements during the PBF-LB process are dynamic, rather than static, the solidification behavior at the end of each laser vector is not constant. In some single tracks, it was observed that the keyhole had closed and only a minor dent or no trace of the keyhole is visible at the top surface after solidification. In some others (Fig. 10 (d, e, h)), it was observed that the keyhole had closed from the middle, but the keyhole bottom had remained open during solidification and hence a defect in the form of the pore is left behind under the solidified surface, similarly as observed with real-time x-ray imaging of the keyhole closing and pore formation by Zhao et al. [32] when the laser was turned off. Such defects are similar in appearance and in formation mechanism to the defects labelled as keyhole pores in previous studies for PBF-LB [33,34] and laser welding [35], with the difference that here they only form at the end of the laser vector, not along the whole vector length, which is the case in those previous studies when operating with process parameters that lead to an unstable keyhole. In this study, within the process parameters operated, the keyhole is stable, and the keyhole defects are formed only at the ends of the laser vectors, not along the whole length of the weld.

As a consequence of such openly or partially-openly solidified keyholes at the ends of the laser vectors, the authors believe that defects are formed and remain in the bulk of the material even after subsequent layers being melted above in two possible ways. 1) the middle of the keyhole closes and solidifies, but the bottom remains open and a pore is formed below the surface (as in Fig. 10 (d, e, h)). As such pore is situated at the very bottom of the penetration depth, the laser tracks of the next layer, having a similar penetration depth but offset higher by the layer thickness, would not remelt all the way down to the depth of the defect, and hence it remains. 2) When the keyhole solidifies completely open (as in Fig. 10 (c, f, g)), during the next powder spreading cycle the powder would try to fill this void. Where the openly solidified keyhole is smaller than the particle size of the powder, the powder would not be able to fill

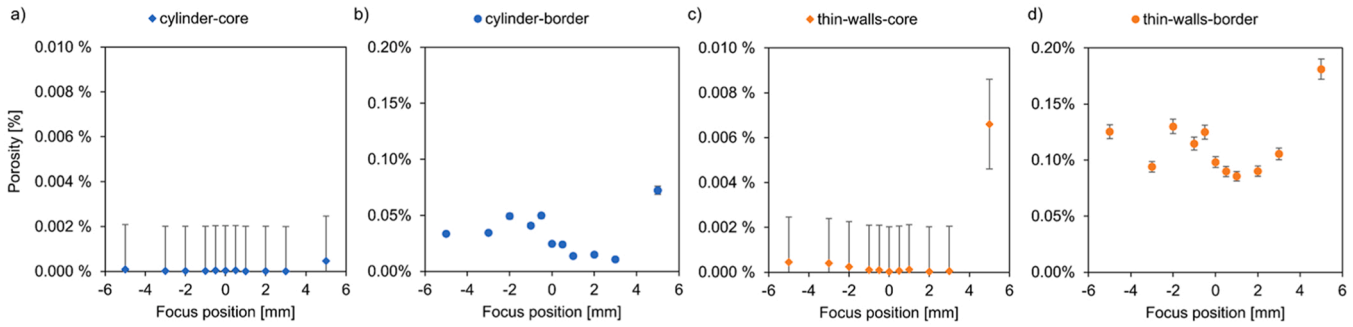

Fig. 8. Calculated porosity for the core (a, c) and border (b, d) regions in the cylinder (a–b) and thin walls (c–d) sections of the specimens. The defects in an area within 0.15 mm distance from the part edge has been assigned as border defects, the rest as core defects.

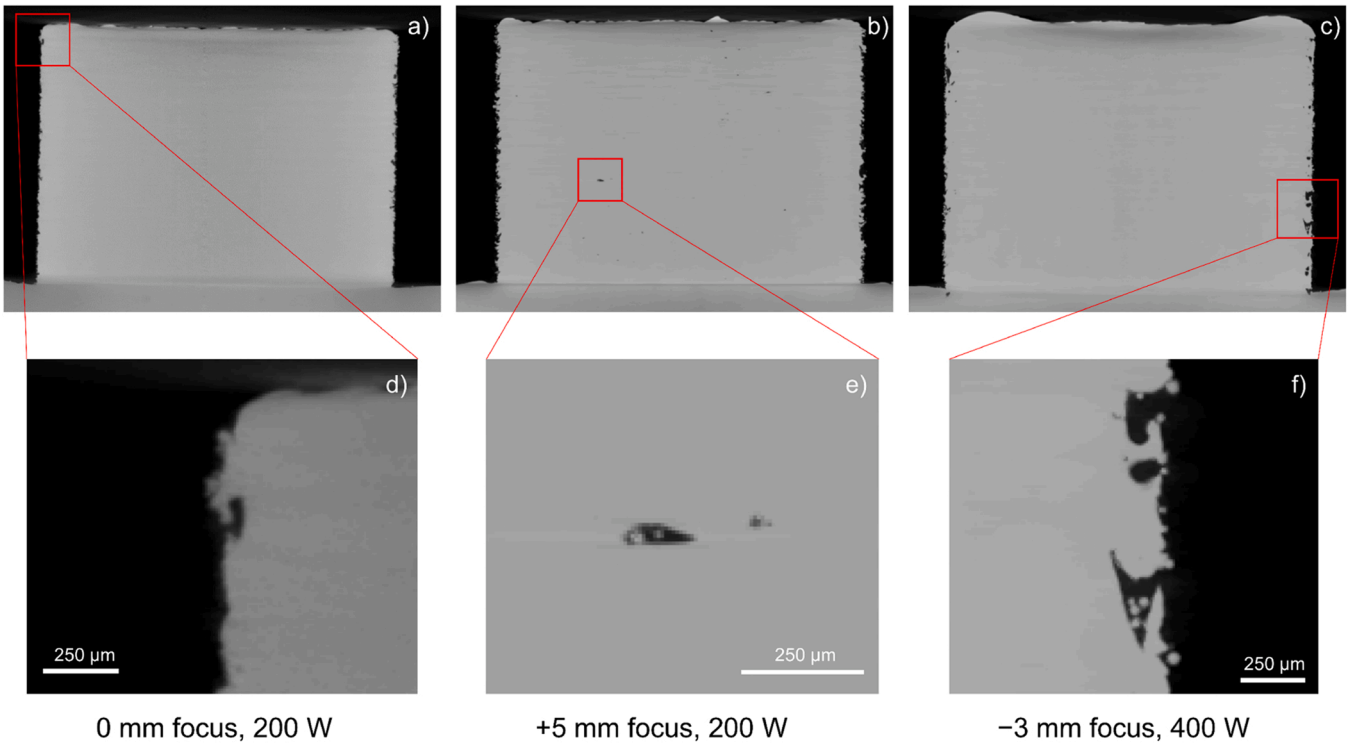

Fig. 9. A typical slice from xCT data for the thin-walled section of (a) specimen 6, produced with nominal laser parameters, (b) specimen 11, produced with +5 mm focus position, and (c) specimen 17, produced with −3 mm focus position and increased laser power of 400 W. (d–f) highlight with higher magnification the typical defects found in the corresponding specimens.

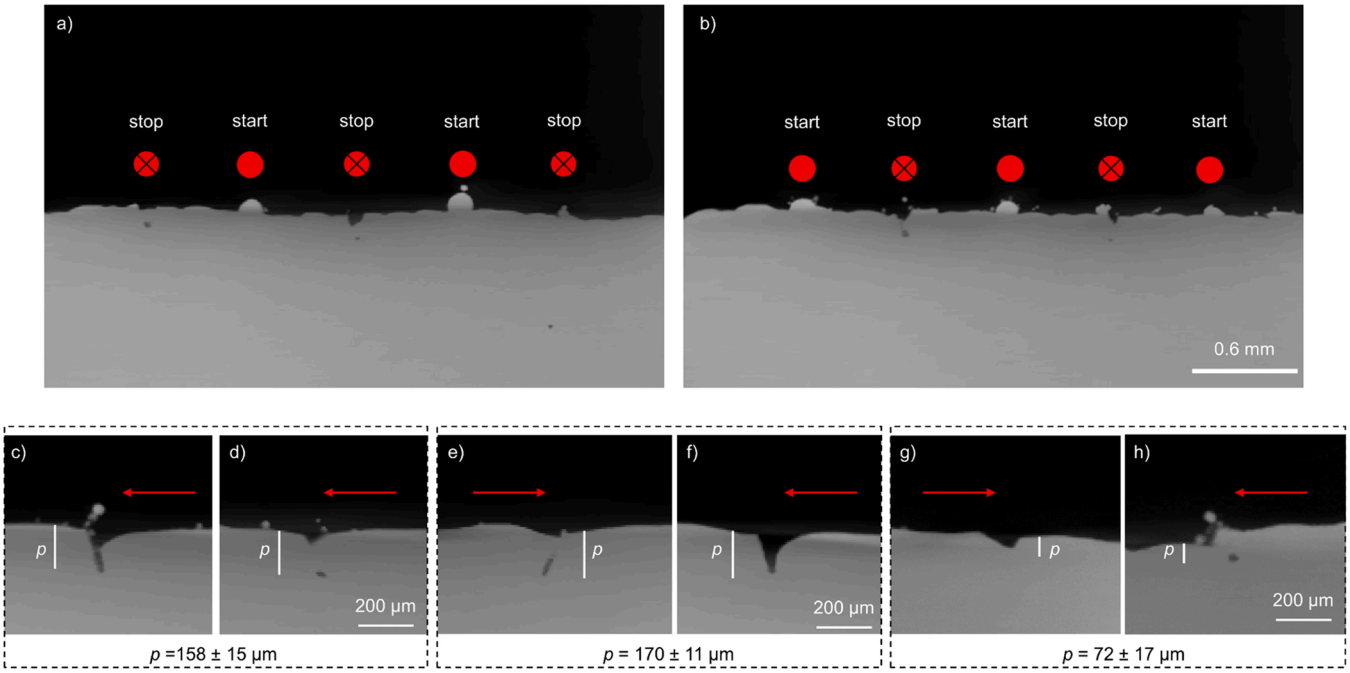

Fig. 10. (a–b) openly solidified keyholes and keyhole pores at the stops (never at the starts) of laser vectors; examples of (c, f, g) keyholes openly solidified all the way to the surface; and in (d, e, h) only the bottom of the keyhole has solidified open, forming a subsurface pore. The red arrows mark the scanning direction, and the white vertical lines mark the average and standard deviation of penetration p as measured from the middle of the corresponding single-track cross-sections.

the void, hence a defect may form during the next laser melting cycle. If the powder would fill the void, the effective thickness of the powder layer at that specific location would be increased, and more importantly, even if there would be powder at the bottom of the previously openly solidified keyhole, the penetration depth of the next layer would not be sufficient to re-melt it, hence a defect filled with unmolten powder particles may form. Un-molten particles were observed in the xCT data at some of the defects found at the edges of the specimens (see Fig. 9(f), which could be an indication of such defect. These plausible defect formation mechanisms are schematically illustrated in Fig. 11.

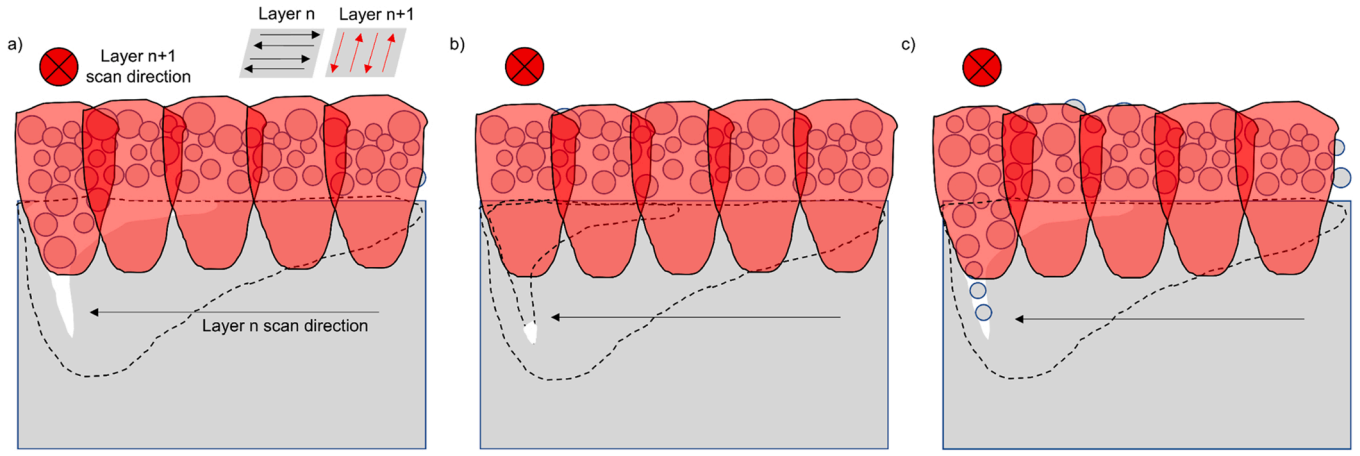

Fig. 11. Schematic illustration of the hypothesized defect formation due to openly solidified keyholes at the laser vector endings; (a) whole keyhole solidified open, (b) just the bottom of the keyhole solidified open, and (c) openly solidified keyhole filled with powder.

Regarding such defects concentrated on the part edges, a potential remedy could be to apply an additional, continuous border scan vector to re-melt around the part contour during the same layer after the core hatching. Although not studied here, it is envisioned that this could effectively remelt and eliminate some of the defects. In this study, the core hatching vector length was set so it is always longer than the part cross-section (>10 mm); hence, in the scan strategy, no laser vector end points are within the core, only at the borders. However, it is known that for larger parts it is beneficial or even required to limit the vector length to reduce and homogenize residual stresses (known as island or chessboard scan strategy). In such scan strategies, it is expected that the openly solidified keyholes at the laser vector endings could lead to similar defects as observed here in the borders and ends of the single-tracks, to be introduced also in the core at the interfaces of the island scans.

3.5. Melt pool monitoring

Finally, it was analyzed how the melt pool monitoring signal response changed along with a change in focus position. Fig. 12 (a) shows the TEP high and TEP low signal intensity as a function of the focus position and beam diameter at the work plane. It can be seen that the signal intensity, both for the TEP low and TEP high sensors, correlates well with the trend in beam diameter, caused by the change in focus position. Fig. 12 (b) further plots the TEP ratio as a function of the focus position. It is interesting to notice, that although the TEP ratio also inversely follows the trend of the curve of the beam diameter to some extent, the individual TEP low and high signal behavior is a better match. The individual, narrow band photodiode signals seem to be useful process monitoring indicators in addition to the ratio, as suggested by [36]. When the laser is in focus, or close to it (within ± 1 mm), the photodiode signals remain essentially constant. Once shifted more than this to either the positive or negative direction, the TEP low and high signal increases correspondingly. When the laser beam is focused to the positive direction (i.e., below the work plane), the TEP high and low signals increase with slightly steeper gradient. This is in good agreement with the change in beam diameter, which also has a slightly asymmetric behavior relative to the focus position, namely the beam diameter increasing with steeper gradient when focus is shifted to the positive direction.

Fig. 12 (c) similarly shows the TED signal as a function of focus position and beam diameter. From −5 to 0 mm there seems to be a linear decrease in the signal intensity, then the lowest value is reached at focus 0 mm, and again the signal intensity starts to increase when moving to positive focus positions. Although, in general, the trend is similar to that of the TEP high and low signals, there are two data points that deviate from the trend. At focus position +0.5 mm, the TED signal jumps higher and deviates from the general trend. This data point (Specimen number 7 in Table 1 and Fig. 2(a)) was identified to be an anomaly caused by a location-depended change in photodiode intensity close to the middle of the building platform, and has to be excluded from the analysis, as elaborated in Appendix B. This data point has been marked with a red circle to the Fig. 12 (c). Then, at focus position +5 mm, the TED signal no longer increases, but rather is decreased to a lower value than at

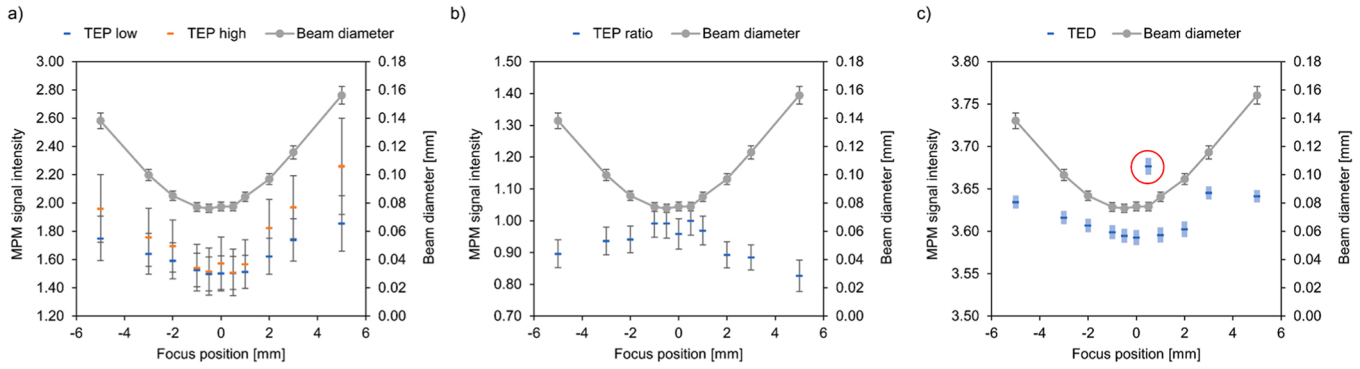

Fig. 12. Correlation of (a) TEP high and TEP low, (b) TEP ratio, and (c) TED with focus position and beam diameter. For the MPM signals, the line marks the mean, transparent colored error bar is the 99% confidence interval of the mean, and the whiskers are the sample standard deviation (which is not shown for TED due to the scale). The number of samples for calculating the TEP high, TEP low and TED statistics was $n = 3035$. The red circle in (c) marks Specimen 7, identified as an anomaly in the TED sensor data (see Appendix B).

+3 mm. Looking closely at the Fig. 12 (a), a slight decrease in the gradient increase of the TEP low (but not TEP high) signal is also seen once moving from focus position +3 to +5 mm, which could be an indication of the same phenomenon. As seen earlier in Fig. 4, in the +5 mm focus position the melt pool depth is lowest, and the width highest, of the studied focus positions. When the beam diameter at work plane increases along with the focus position change, the melt pool width increases and the depth decreases due to the reduced laser power density [J/mm^2]. With decreasing laser power density, the melt pool peak temperature decreases [37] and vapor plume formation reduces [38]. The interplay of these three conditions, namely 1) melt pool temperature, 2) melt pool size and 3) vapor plume, and how effectively it is removed from above the melt pool by the shielding gas flow, will all have an influence on the photodiode signal. Detailed study of this interplay is beyond the scope of this study and part of another on-going study. Nevertheless, it is believed that the behavior of the photodiode signals at the +5 mm focus position can be explained by the interplay of these effects, and at that point a transition in the conditions at the melt pool is occurring.

About the TED signal, it must be further noted that the changes in the average signal intensities between the studied focus positions are very small (but nevertheless statistically significant as indicated by the 99% confidence intervals as error bars) compared to the corresponding changes in the TEP high and low signals. This has been identified to be due to significant laser back-reflection reaching the TED photodiode sensor (see Appendix B) and hence only a small portion of the signal intensity is due to thermal emissions from the melt pool. The TEP high and low photodiodes have narrow band filters in from of them, which (although not placed there specifically for that reason), reduce the effect of the laser back-reflection. As seen in Appendix B. Fig. B.3, in the TEP high sensor location the 1070 nm peak corresponding to the laser back-reflection is negligible, whereas for TEP low there is minor contribution

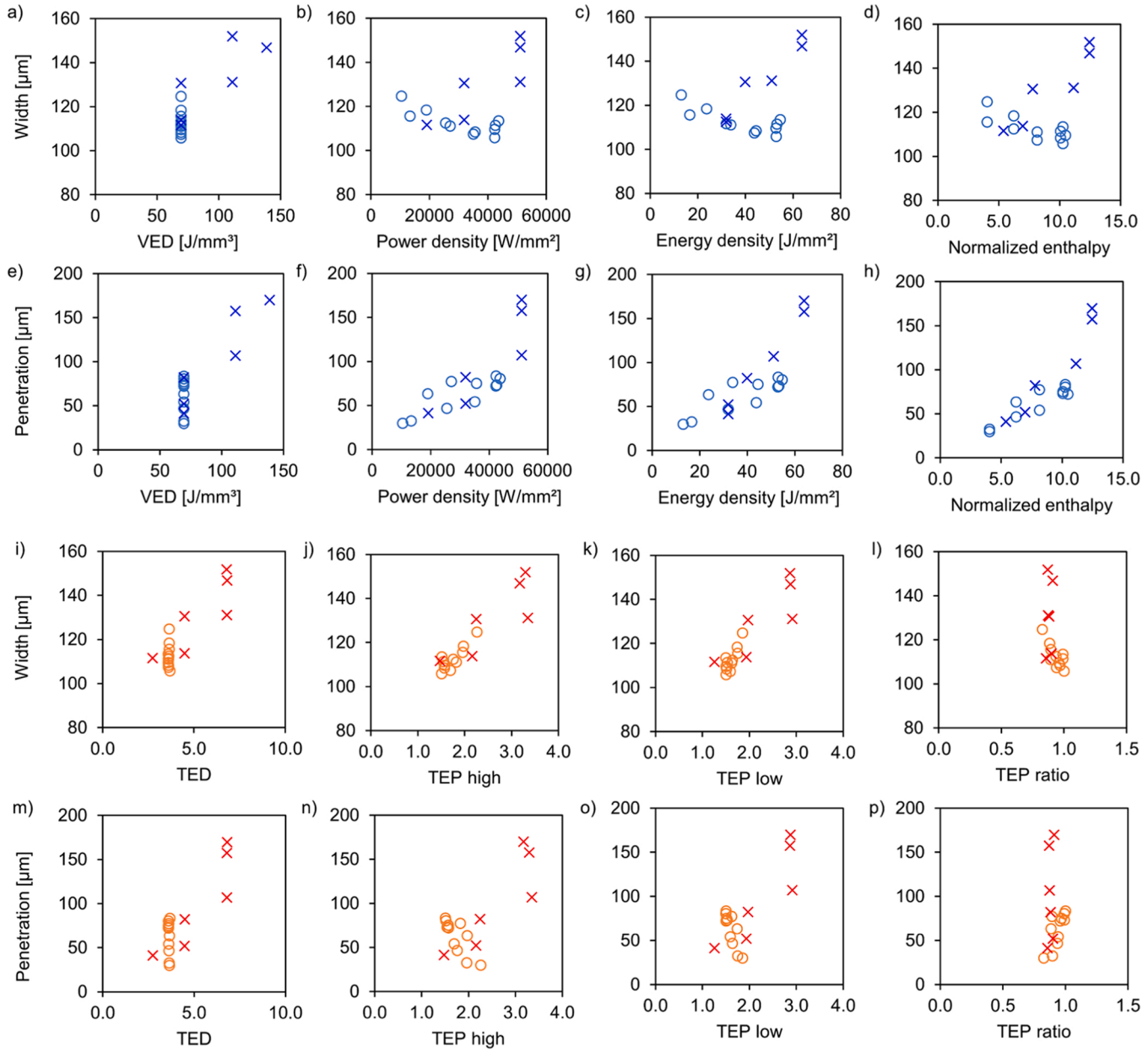

Fig. 13. Melt pool width (a–d) and (i–l) and melt pool penetration (e–h) and (m–p) as a function of energy density parameters (blue) and MPM signals (orange). Circles mark the specimens with varying focus position, while crosses mark specimens with constant focal point position but varying laser power, speed, and hatch distance.

and then for the TED sensor the 1070 nm peak already dominates.

The melt pool monitoring system, especially via the TEP high signal, seems to be an effective way to identify changes in focus position. This could be used to monitor focus shift caused by thermal lensing due to dirt on or degradation of the optics, which is common in PBF-LB systems.

In addition to the specimens where focus position was varied (1−11), the designed experiment included specimens produced with different combinations of laser parameters (12−17), yielding different energy densities, as seen in Table 1. The purpose of this, along with the focal point position change, was to study how the energy density parameters correlate with the melt pool width and depth in a situation where the focus position (and beam diameter) is included as a variable. Furthermore, it was postulated as to whether the melt pool monitoring signal could work as similar energy density metric for capturing the compound effect of all the individual input parameters. For this purpose, the melt pool dimensions as a function of the energy density parameters and the melt pool monitoring signals are plotted. The results are presented in Fig. 13. The specimens made with varying focus position are marked with circles. The specimens where the focus remains constant, but other laser parameters were changed, are marked with crosses. Some interesting observations can be made. For *VED,* the focus position and by extension, the resulting beam diameter, is not included in the metric calculation, hence all the responses marked with circles are at the same x-axis location. Due to this, *VED* is an essentially useless descriptor of the forming melt pool dimensions when the focus position (and resulting beam diameter) is included as a variable. For power density, energy density, and normalized enthalpy, there seem to be diverging behavior in melt pool width and penetration response between the specimens where the focus position is varied, compared to those where only the other process parameters are changed. The same behavior is even more evident when plotting penetration depth and weld width as a function of the MPM signal intensities.

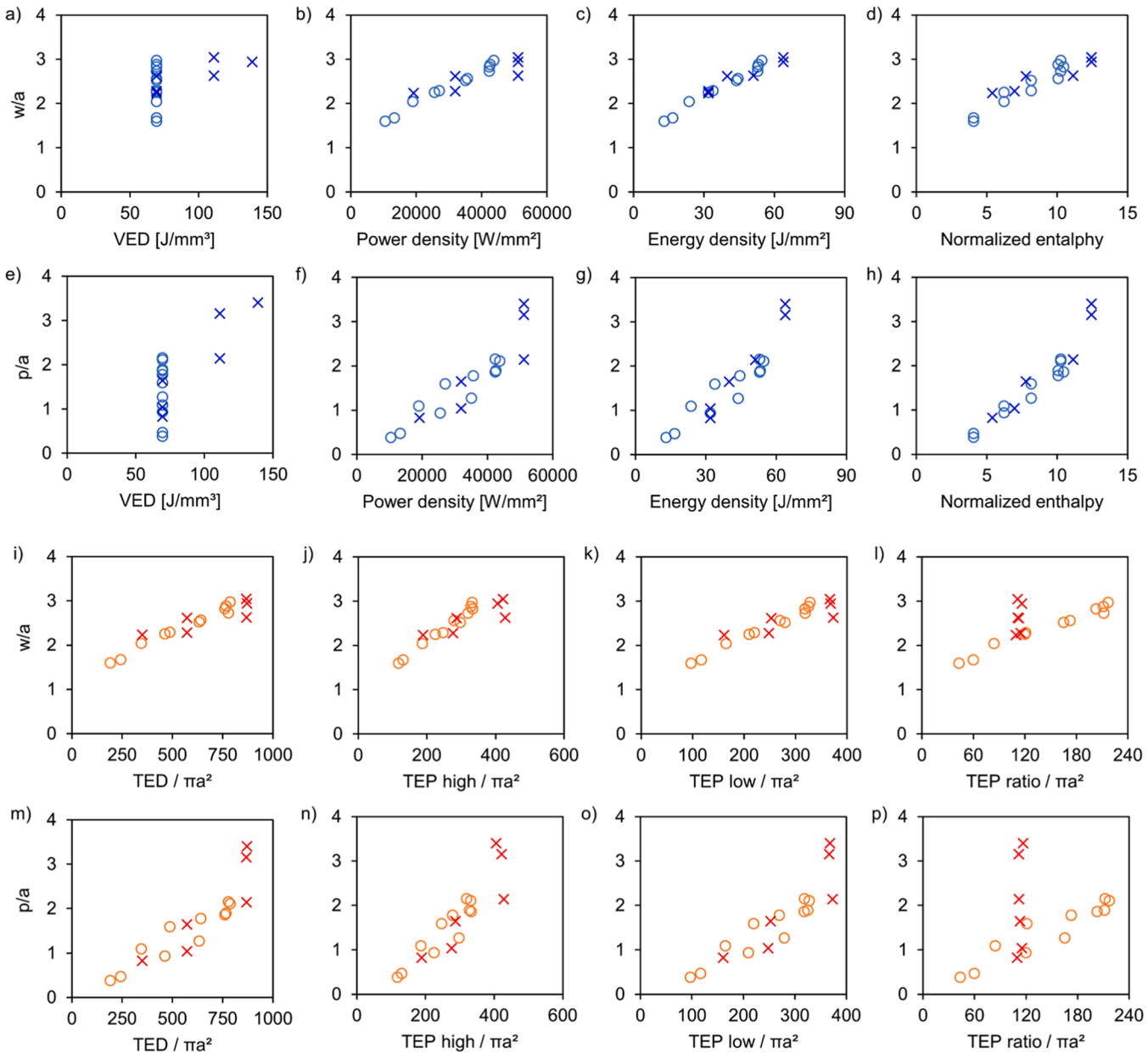

Fig. 14. Melt pool width (a−d) and (i−l) and melt pool penetration (e−h) and (m−p) normalized with beam radius *a*, as a function of energy density parameters (blue) and MPM signals (orange). Circles mark the specimens with varying focus position, while crosses mark specimens with constant focal point position but varying laser power, speed, and hatch distance.

This behavior with a changing beam diameter has been identified in previous studies involving the use of normalized enthalpy [13,39]. Because of this, the responses corresponding to melt pool depth and width are usually also normalized with the beam size. In Fig. 14, the penetration depth and width are divided by the beam radius to get normalized width $w^* = w/a$ and normalized penetration depth $p^* = p/a$. Furthermore, in Fig. 14, we have normalized the MPM signals by dividing the signal intensity with the beam area term (πa^2), which is the same term used to characterize the beam size in the metrics *PD*, *ED,* and $\Delta H/hs$. With this, the data collapses much closer to a linear curve for all the used metrics, except VED and the TEP ratio. For VED, this is to be expected, as the metric does not contain a term for characterizing the beam size. For the TEP ratio, a clear diverging behavior is observed between the circles, where the focus position changes, and the crosses, where focus remains constant. When the focus position is changed, the normalized TEP ratio follows a similar trend as the other metrics; however, the crosses that correspond to data points where the focus position (and hence beam diameter) remains constant, but the other parameters are changed, have a totally different response. Providing a definite explanation for this observation is beyond the scope of this study. Nevertheless, it is believed this is also a manifestation of the interplay between the mixed effects of 1) melt pool temperature, 2) melt pool area and 3) vapor plume, which all have an influence on the spectral emissions captured by the photodiode, and which are all affected by a change in the processing parameters. Further studies would be needed to identify the relationship and quantify the magnitude of each process parameter on the photodiode signals, individually and with taking into consideration combinatorial effects.

It can be also noticed, that a deviation for the penetration depth from the linear trend starts to occur for the two data points having the highest normalized enthalpy of $\Delta H/hs$ ~12. This agrees with the transition identified by Hann et al. [13] at around $\Delta H/hs \sim 10$. This is due to the sharp increase in absorptivity once a transition from conduction to fully developed keyhole mode occurs. Note that in $\Delta H/hs$, the absorptivity is modeled as a constant, set at 0.4 in this study. King et al. [40] identified the transition to $\Delta H/hs \sim 30$, but the differences in the absolute values might be due to different values for the input constants used. In recent studies by Naderi and Weaver et al. [39,41], on the fidelity of more advanced scaling laws, all of which consider the dimensionless parameter $\Delta H/hs$, for the PBF-LB developed by Rubenchik et al. [37], Ye at al. [42], and Fabbro [43], they have found that the errors in predicting the melt pool depth based on such scaling laws are still in the order of 50−100% (reduced to 35% when incorporating a non-constant absorption coefficient). Even with the obvious challenges in predicting the absolute value of the response with very high accuracy, the models based on the concept of normalized enthalpy seem to capture the underlying trend in the resulting normalized melt pool depth and width when different combinations of the input parameters are considered. Based on the findings of this study, this is also true in situations where the focus position (and resulting beam diameter) change is included as a variable. Similarly, it was found in this study that normalizing the MPM photodiode signals TEP high, TEP low, and TED with the beam area at the work plane collapses the normalized melt pool dimensional response towards a linear curve. This indicates possibilities for utilizing such photodiode-based process monitoring signals as a new way to capture the total energy density of the PBF-LB process and use it for assessing the resulting melt pool geometry when the combination of process parameters are varied.

In this study, the correlation between the MPM signals and porosity formation as a function of the process parameters was not studied. The authors have considered melt pool geometry to be a more fundamental unit indicator of a change in melting conditions than porosity. Melt pool geometry more directly shows whether there is an impact on the melting conditions. This impact then may or may not lead to porosity, such as lack of fusion or keyhole porosity, or even spattering related porosity, all of which are derivates of a change in melting conditions. Keyhole porosity is the result of unstable/too deep melt pool, whereas lack of fusion would be the result of too narrow or too shallow melt pool. A change in melt pool dimensions then may or may not lead to a change in porosity. Linking the photodiode response directly to porosity would be *indirect*, a surrogate acting through the melt pool conditions. The authors see no physical reason why the photodiode signal would *directly* correlate with porosity formation. It is, however, clear why a change in melt pool dimensions (or temperature, or other melting conditions) would directly correlate with the photodiode signal, because that directly impacts on the amount and energy of the photons that are emitted from the melt pool and reach the photodiode.

4. Conclusions

A comprehensive study of the effect of laser focus position on porosity and melt pool geometry in PBF-LB AM was conducted. For this purpose, specimens with cylindrical, thin-walled, and single-track features were designed and produced with varying laser focus positions and laser energy densities. Melt pool geometry and porosity was measured with optical microscopy from cross-sections. X-ray computed tomography was used to conduct a more comprehensive analysis of the porosity to extract pore sizes and spatial distribution within the specimens. In addition, the capabilities of using melt pool monitoring with co-axial photodiodes as a method to capture changes in the melting process caused by the shifting laser focus was studied. Based on the findings of this study, the following conclusions can be drawn:

1. Laser beam focal point position has a significant effect on the melt pool depth in PBF-LB, which decreased dramatically when the focal point position is shifted in either a positive or negative direction by more than ± 1 mm (with a beam with Rayleigh length of ~3 mm). The penetration was reduced already by more than 50% when focus was shifted by +5 mm. Within the studied range of focus positions, the effects on the melt pool width were more subtle. The average melt pool width showed a slight increase when shifting the focal point position to either direction. Due to small differences in the weld widths, and relatively small sample size of 5 measurements, no statistically significant difference between the averages of the weld widths can be concluded with high confidence.
2. The total porosities within the cylinders were extremely low at ≤0.004% as measured from x-CT data for all the studied focus positions. For the thin walls, there was, on average, a 10-fold increase in the total porosity, due to increased contribution of border porosity. When the focus is above the work plane, between −5 and −0.5 mm, the total porosity remains relatively constant. Once on focus and slightly below the work plane between 0 and +2 mm, there is even a slight decrease in porosity. A significant increase in the number of pores was seen only once the focus was shifted by up to +5 mm, a condition where the penetration depth also reached its lowest value. In this condition, irregularly shaped pores with unmolten particles within started to emerge in the core of the thin-walled geometries. This would indicate stochastic, but not yet systematic, appearance of lack-of-fusion porosity due to the severe loss of penetration in this condition.
3. Formation of defects due to openly solidified keyholes was identified to occur at the ends of individual laser vectors in the single scan-tracks. Increasing the laser power resulted in increased occurrence of such defects. Such defects were formed as part of the scanning strategy, when the laser is turned off, and the keyhole that was present had remained open due to the extremely rapid solidification, surpassing the speed at which the molten metal could fill and close the keyhole. Both completely open, and partially openly solidified keyholes were observed. From the xCT data, it was seen that most of the pores are concentrated on the edges of the specimens (i.e., border porosity), regardless of the focus position. The authors provide a hypothesis that these defects concentrated on the edges may be, at

least in part, due to the openly solidified keyholes identified from the single tracks.

4. Melt pool monitoring using co-axial photodiodes was able to capture the change in melting conditions caused by a change in the focus position (and resulting change in beam diameter), and the signal response had a similar trend with the corresponding change in melt pool penetration. The laser beam diameter, melt pool monitoring signal, melt pool penetration and to a lesser extent, width, all follow a similar trend over the beam caustic as the focus position is changed.
5. Of the studied energy density parameters, volumetric energy density was found to be ineffective in predicting the resulting normalized melt pool geometry when the focus position (and resulting change in beam diameter) is included as a variable. This is to be expected, as the VED metric does not include any term characterizing the beam size. Plotting against normalized enthalpy, the data for both normalized weld width and penetration collapsed very close to a linear curve, as observed also in previous studies utilizing the normalized enthalpy. Within the parameter range explored in this study, even the simpler metrics of power density and energy density worked reasonably well. This was to be expected, as within this study the material (316 L) remained constant. The main difference of the normalized enthalpy compared to the simpler metrics is the addition of material-related parameters and hence expanding the applicability of the metric to encompass the used material as variable.
6. Normalizing the MPM photodiode signals with the laser beam area on a work plane produced a linear response on the melt pool width and penetration within the parameter range studied. Using the normalized photodiode signals as a combined energy density metric seems like a new potential way to reduce the input parameters (laser power, speed, beam diameter, and hatch distance) to a single metric that correlates with the resulting melt pool geometry. Similar to the normalized enthalpy, the transition between conduction and fully developed keyhole melting mode could be inferred as the point where the linear trend breaks down. Instead of a predictive metric, this could provide a means to continuously monitor the melting process and identify dynamic, unwanted events which lead to deviation in the melt pool geometry, and eventually, part quality.

Regarding the focus shift during PBF-LB of 316 L, a tolerance limit of ±1 mm (or 30% of Rayleigh length) is recommended to limit the variation in melt pool penetration to less than 13%, which is comparable with the intra-specimen variation (10−23%) observed within a specific focus position on this range. As this study was conducted on one alloy, one machine and scanning parameters for 30 μm layer thickness, further studies are needed to assess whether the recommendation could be generalized to encompass various alloys and related scanning strategies. Focus shifts larger than this result in a dramatic loss of penetration and were effectively captured by the TEP high and TEP low signals in the melt pool monitoring system, indicating the potential of using such photodiode-based melt pool monitoring systems for continuous monitoring of focus shift in PBF-LB AM. Regarding the initial findings made in this study on using MPM signals as universal predictors of the resulting melt pool geometry in PBF-LB, more rigorous studies are still needed on the behavior of the photodiode signal response (and which spectral regimes should be observed) as a function of the varying input parameters.

CRediT authorship contribution statement

Joni Reijonen: Writing – review & editing, Writing – original draft, Visualization, Software, Methodology, Investigation, Formal analysis, Conceptualization. **Antti Salminen:** Writing – review & editing, Supervision. **Alejandro Revuelta:** Writing – review & editing, Software, Methodology, Formal analysis. **Sini Metsä-Kortelainen:** Writing – review & editing, Supervision, Funding acquisition, Conceptualization.

Declaration of Competing Interest

The authors declare that they have no known competing financial interests or personal relationships that could have appeared to influence the work reported in this paper.

Data Availability

Data will be made available on request.

Acknowledgements

The financial support of VTT Technical Research Centre of Finland is gratefully acknowledged. The authors would like to thank Kimmo Ruusuvuori from VTT for the operation of the PBF-LB machine, Hanna Iitti from VTT for the preparation of metallographic specimens and Jukka Kuva from GTK for xCT, which is supported by the Academy of Finland via RAMI infrastructure project (#293109). Joni Reijonen is grateful to Walter Ahlström Foundation (Grant number 20240108) for supporting this work.

Appendix A. Scanning orientation in the experiment

To allow for reproducibility of the experiments, the scanning strategy, specifically the orientation of the scanning vectors and how they were rotated per each layer in the build job, is listed in Table A.1. The coordinate system as to which the angles related to, is shown in Fig. 2(b) bottom left corner.

Table A.1. Orientation of scanning vectors for each layer in the build job, in relation to the y-axis as shown in Fig. 2(b).

Layer no.	Angle [deg]	Layer no.	Angle [deg]	Layer no.	Angle [deg]	Layer no.	Angle [deg]	Layer no.	Angle [deg]	Layer no.	Angle [deg]	Layer no.	Angle [deg]
1	35	56	-40	111	-25	166	-10	221	5	276	20	331	35
2	-22	57	-7	112	8	167	23	222	38	277	-37	332	-22
3	11	58	26	113	41	168	-34	223	-19	278	-4	333	11
4	44	59	-31	114	-16	169	-1	224	14	279	29	334	44
5	-13	60	2	115	17	170	32	225	-43	280	-28		
6	20	61	35	116	-40	171	-25	226	-10	281	5		
7	-37	62	-22	117	-7	172	8	227	23	282	38		
8	-4	63	11	118	26	173	41	228	-34	283	-19		
9	29	64	44	119	-31	174	-16	229	-1	284	14		
10	-28	65	-13	120	2	175	17	230	32	285	-43		
11	5	66	20	121	35	176	-40	231	-25	286	-10		
12	38	67	-37	122	-22	177	-7	232	8	287	23		

(*continued on next page*)

(*continued*)

Layer no.	Angle [deg]	Layer no.	Angle [deg]	Layer no.	Angle [deg]	Layer no.	Angle [deg]	Layer no.	Angle [deg]	Layer no.	Angle [deg]	Layer no.	Angle [deg]
13	-19	68	-4	123	11	178	26	233	41	288	-34		
14	14	69	29	124	44	179	-31	234	-16	289	-1		
15	-43	70	-28	125	-13	180	2	235	17	290	32		
16	-10	71	5	126	20	181	35	236	-40	291	-25		
17	23	72	38	127	-37	182	-22	237	-7	292	8		
18	-34	73	-19	128	-4	183	11	238	26	293	41		
19	-1	74	14	129	29	184	44	239	-31	294	-16		
20	32	75	-43	130	-28	185	-13	240	2	295	17		
21	-25	76	-10	131	5	186	20	241	35	296	-40		
22	8	77	23	132	38	187	-37	242	-22	297	-7		
23	41	78	-34	133	-19	188	-4	243	11	298	26		
24	-16	79	-1	134	14	189	29	244	44	299	-31		
25	17	80	32	135	-43	190	-28	245	-13	300	2		
26	-40	81	-25	136	-10	191	5	246	20	301	35		
27	-7	82	8	137	23	192	38	247	-37	302	-22		
28	26	83	41	138	-34	193	-19	248	-4	303	11		
29	-31	84	-16	139	-1	194	14	249	29	304	44		
30	2	85	17	140	32	195	-43	250	-28	305	-13		
31	35	86	-40	141	-25	196	-10	251	5	306	20		
32	-22	87	-7	142	8	197	23	252	38	307	-37		
33	11	88	26	143	41	198	-34	253	-19	308	-4		
34	44	89	-31	144	-16	199	-1	254	14	309	29		
35	-13	90	2	145	17	200	32	255	-43	310	-28		
36	20	91	35	146	-40	201	-25	256	-10	311	5		
37	-37	92	-22	147	-7	202	8	257	23	312	38		
38	-4	93	11	148	26	203	41	258	-34	313	-19		
39	29	94	44	149	-31	204	-16	259	-1	314	14		
40	-28	95	-13	150	2	205	17	260	32	315	-43		
41	5	96	20	151	35	206	-40	261	-25	316	-10		
42	38	97	-37	152	-22	207	-7	262	8	317	23		
43	-19	98	-4	153	11	208	26	263	41	318	-34		
44	14	99	29	154	44	209	-31	264	-16	319	-1		
45	-43	100	-28	155	-13	210	2	265	17	320	32		
46	-10	101	5	156	20	211	35	266	-40	321	-25		
47	23	102	38	157	-37	212	-22	267	-7	322	8		
48	-34	103	-19	158	-4	213	11	268	26	323	41		
49	-1	104	14	159	29	214	44	269	-31	324	-16		
50	32	105	-43	160	-28	215	-13	270	2	325	17		
51	-25	106	-10	161	5	216	20	271	35	326	-40		
52	8	107	23	162	38	217	-37	272	-22	327	-7		
53	41	108	-34	163	-19	218	-4	273	11	328	26		
54	-16	109	-1	164	14	219	29	274	44	329	-31		
55	17	110	32	165	-43	220	-28	275	-13	330	2		

Appendix B. Characterization of the photodiode sensor signals

During the analysis of the experimental results, it was noticed that Specimen number 7, corresponding to the focal point position condition of +0.5 mm in the experiment, had a significantly differing response in the TED sensor signal, compared to the others. Additional experiments were made to assess the sensor signal uniformity across the whole active build area to identify the root cause for the anomaly. A 120×120 mm area (excluding the corners with the bolt holes, see Fig. 2a) with constant laser parameters (No. 6 in Table 1.) was scanned and the sensor signals collected. The results are plotted in Fig. B.1, where (a−c) maps the signal intensities in XY-space for one layer, and (d−f) shows the histograms of the data respectively. It can be seen, that the sensor signals are very uniform across the build area, except for the center of the build plate, where the signal intensity is increased on a semi-circular area. Let's refer to this anomaly as central halo for now. After revisiting the data of the actual experiment, it was found that the Specimen 7 (corresponding to the +0.5 mm focal point position condition) was placed within the area of influence of this central halo, but only for the TED sensor. The intensity is higher and the radius larger for this central halo in the TED sensor, compared to the TEP high and low sensors. In the TEP high sensor, the central halo is barely visible. The extended radius of this central halo for the TED sensor can be best seen in Fig. B.2. There, it can be seen that only for the TED the central halo extended to the Specimen number 7 location. The TED data point in Fig. 12 (c) corresponding to focal point position +0.5 mm is therefore considered an anomaly and hence deviates from the general trend. This has been marked with a red circle in the figure.

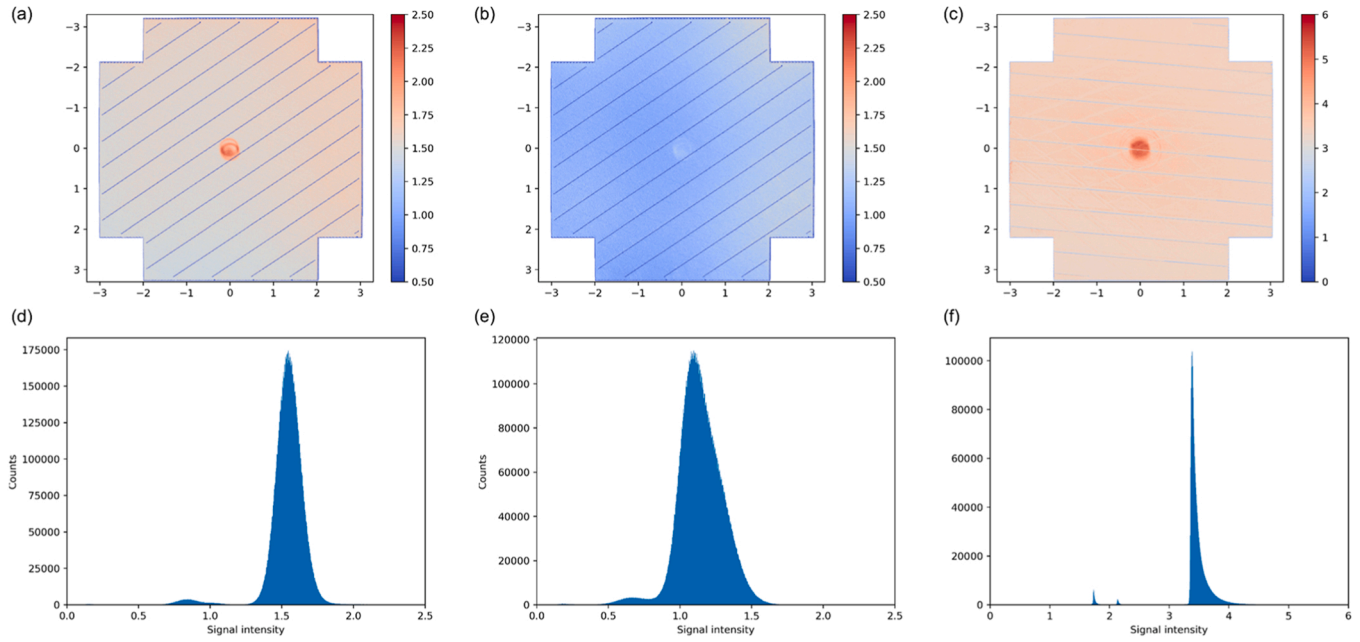

Fig. B.1. Signal intensities across the build platform for (a) TEP LOW, (b) TEP HIGH and (c) TED sensors. The diagonal line patterns in (a–c) are due to the scanning pattern; the signal being lower at the vector beginnings as the laser is heating the material, prior melt pool forms and stable conditions are reached. The corresponding histograms of the data are shown in (d–f), when scanning with constant laser parameters.

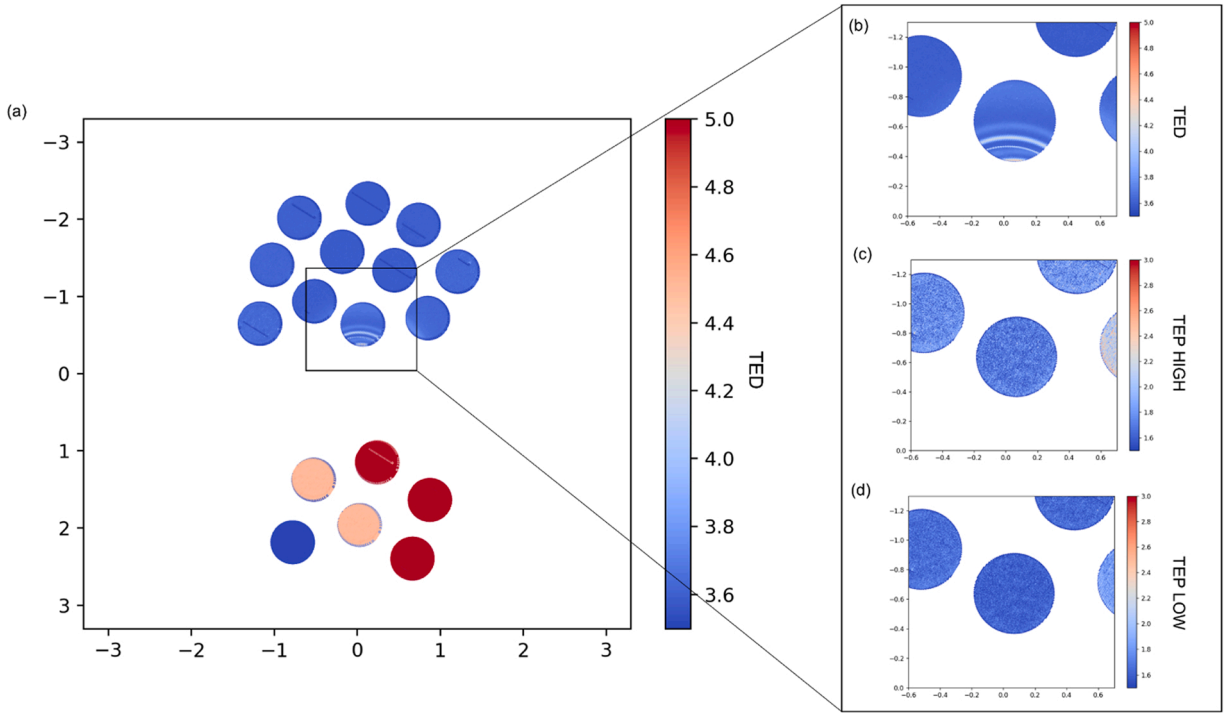

Fig. B.2. (a) TED photodiode signal intensity for the whole build area of layer number 50 in the actual experiment, with a close-up of Specimen 7 location with (b) TED, (c) TEP HIGH and (d) TEP LOW signal intensities. As can be seen, only in the TED sensor signal the influence of the central halo extents to the Specimen 7 location.

The root cause of this central halo was suspected to be increased laser back-reflection at the center location, compared to the rest of the build area. When laser scanning at the middle, the angle of incidence of the laser beam is close to zero, hence increased back-reflection could be directed through the optical path and to the photodiode sensors. However, nominally according to the specification, the beam splitter should be passing light only between wavelengths 450–900 nm, and furthermore, the TEP sensors have narrow band filters (TEP low 636 ± 5 nm and TEP high 650 ± 5 nm) in front of them and should exclude the laser wavelength of 1070 nm. However, it was suspected that the optical components may not be perfect and the laser back-reflection could still contribute to the photodiode signals. To verify this, an experiment was made where each photodiode was replaced with a spectrometer (Ocean Insight HR4PRO with extended range 200–1100 nm) to acquire the spectrum of the light that is received by each of the photodiode sensors during the laser melting. The same area as described in Appendix A was scanned with constant laser parameters (No. 6 in Table 1.) to collect the spectrometer data individually for each sensor. The results are shown in Fig. B.3. It can be seen that for the TEP high sensor with the 650 ± 5 nm bandpass filter, there is the major peak corresponding to those wavelengths, and an extremely small peak around the 1070 nm laser

wavelenght. However, with the TEP low sensor with the 636 ± 5 nm bandpass filter, the 1070 nm peak is already clearly visible. Furthermore, with the TED sensor where a wide spectrum of light is received (no bandpass filter), the peak corresponding to the laser wavelength at 1070 nm is already dominant. Finally, we tested placing a shortpass filter with a cut-off wavelength at 800 nm in front of the TED sensor path and made the same experiment to verify that the central halo was due to the laser back-reflection and indeed this was the case, as seen on Fig. B.4. where the central halo is absent.

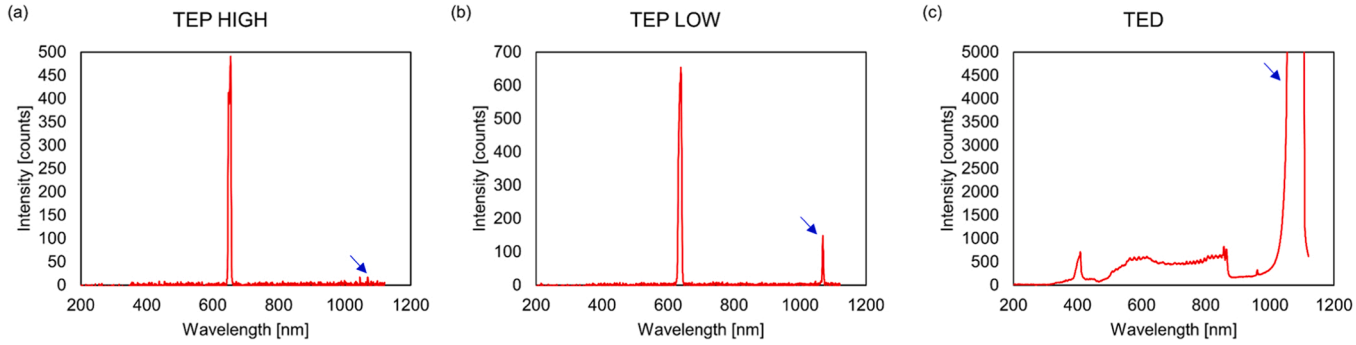

Fig. B.3. Spectral analysis of light received at the ends of (a) TEP HIGH, (b) TEP LOW and (c) TED sensor optical paths while laser melting stainless steel in the original PrintRite3D MPM system configuration, as used in the study. The blue arrows mark the 1070 nm peak, corresponding to the laser wavelength.

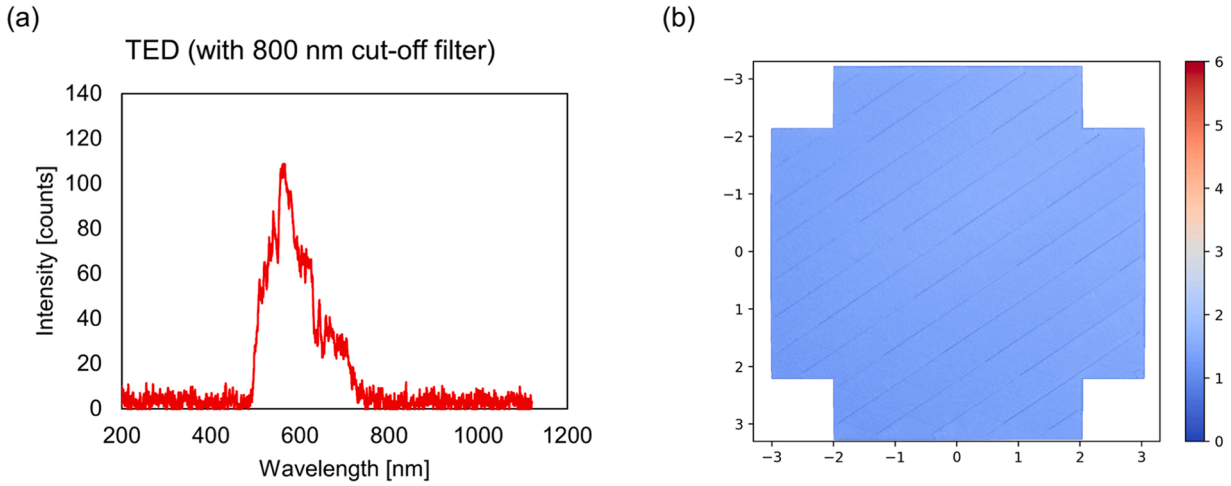

Fig. B.4. (a) spectral analysis and (b) TED sensor signal for the whole build area while applying a shortpass filter with a 800 nm cut-off wavelength in front of the sensor, demonstrating the elimination of the laser wavelength and hence, the central halo.

Appendix C. Calibration state of the machine

Before the experiments of this study, the used PBF-LB machine has been calibrated along with the 12-month interval maintenance by the machine OEM. During the maintenance, focus shift caused by thermal lensing or any other reason is checked and corrected for. This was done by checking the focal point position in relation to the work plane (z-direction), by measuring the beam diameter over the beam caustic with a focus beam profiler (FBP from Cinogy GmbH) to identify the beam waist position in relation to the work plane, and then adjusting the focal point position (by manually adjusting the VarioScan focusing lens position) so that the beam waist is once again at the nominal work plane (defined as 0 mm in this study). This is the starting condition, from which the focus position was then programmatically varied (within −5 to +5 mm) using the VarioScan during the experiments.

The x-y position related correction to maintain the focal plane at the work plane for the whole build area (the so called flat-view correction) is also achieved with the VarioScan, which is a dynamic focusing unit, that can be used as a replacement of the static f-theta lens to do essentially the same job. A programmatic correction file (x-y position and z-correction factor grid) has been generated by the machine OEM during the calibration, which corrects the focal length by adjustment made on the VarioScan optics on the fly automatically, based on the x-y position of the scanner. This maintains focal point position (in the Z-direction) always on the work plane (nominal 0 mm). This is the so called flat-view correction. Then, the adjustments made in this study to the focal point position from +5 to −5 mm are on top of that programmatic correction applied based on x-y scanner position.

Regarding any other property or set parameter (such as laser power, layer thickness or scanning speed) of the machine, the authors trust that the machine manufacturer has properly done the calibration of the machine.

References

[1] A. Keshavarzkermani, E. Marzbanrad, R. Esmaeilizadeh, Y. Mahmoodkhani, U. Ali, P.D. Enrique, N.Y. Zhou, A. Bonakdar, E. Toyserkani, An investigation into the effect of process parameters on melt pool geometry, cell spacing, and grain refinement during laser powder bed fusion, Opt. Laser Technol. 116 (2019) 83–91, https://doi.org/10.1016/j.optlastec.2019.03.012.

[2] J.J.S. Dilip, S. Zhang, C. Teng, K. Zeng, C. Robinson, D. Pal, B. Stucker, Influence of processing parameters on the evolution of melt pool, porosity, and microstructures in Ti-6Al-4V alloy parts fabricated by selective laser melting, Prog. Addit. Manuf. 2 (2017) 157–167, https://doi.org/10.1007/s40964-017-0030-2.

[3] A. du Plessis, Effects of process parameters on porosity in laser powder bed fusion revealed by X-ray tomography, Addit. Manuf. 30 (2019) 100871, https://doi.org/10.1016/j.addma.2019.100871.

[4] A. Leicht, M. Rashidi, U. Klement, E. Hryha, Effect of process parameters on the microstructure, tensile strength and productivity of 316L parts produced by laser powder bed fusion, Mater. Charact. 159 (2020) 110016, https://doi.org/10.1016/j.matchar.2019.110016.
[5] R. Esmaeilizadeh, A. Keshavarzkermani, U. Ali, B. Behravesh, A. Bonakdar, H. Jahed, E. Toyserkani, On the effect of laser powder-bed fusion process parameters on quasi-static and fatigue behaviour of Hastelloy X: a microstructure/defect interaction study, Addit. Manuf. 38 (2021) 101805, https://doi.org/10.1016/j.addma.2020.101805.
[6] S. Siddique, M. Imran, E. Wycisk, C. Emmelmann, F. Walther, Influence of process-induced microstructure and imperfections on mechanical properties of AlSi12 processed by selective laser melting, J. Mater. Process. Technol. 221 (2015) 205–213, https://doi.org/10.1016/j.jmatprotec.2015.02.023.
[7] J. Liu, G. Li, Q. Sun, H. Li, J. Sun, X. Wang, Understanding the effect of scanning strategies on the microstructure and crystallographic texture of Ti-6Al-4V alloy manufactured by laser powder bed fusion, J. Mater. Process. Technol. 299 (2022), https://doi.org/10.1016/j.jmatprotec.2021.117366.
[8] P. Bidare, I. Bitharas, R.M. Ward, M.M. Attallah, A.J. Moore, Laser powder bed fusion in high-pressure atmospheres, Int. J. Adv. Manuf. Technol. 99 (2018) 543–555, https://doi.org/10.1007/s00170-018-2495-7.
[9] J. Reijonen, A. Revuelta, T. Riipinen, K. Ruusuvuori, P. Puukko, On the effect of shielding gas flow on porosity and melt pool geometry in laser powder bed fusion additive manufacturing, Addit. Manuf. 32 (2020) 101030, https://doi.org/10.1016/j.addma.2019.101030.
[10] L. Thijs, F. Verhaeghe, T. Craeghs, J.Van Humbeeck, J.P. Kruth, A study of the microstructural evolution during selective laser melting of Ti-6Al-4V, Acta Mater. 58 (2010) 3303–3312, https://doi.org/10.1016/j.actamat.2010.02.004.
[11] Y. Kawahito, M. Mizutani, S. Katayama, Elucidation of high-power fibre laser welding phenomena of stainless steel and effect of factors on weld geometry, J. Phys. D. Appl. Phys. 40 (2007) 5854–5859, https://doi.org/10.1088/0022-3727/40/19/009.
[12] M.M.A. Khan, L. Romoli, G. Dini, M. Fiaschi, A simplified energy-based model for laser welding of ferritic stainless steels in overlap configurations, CIRP Ann. - Manuf. Technol. 60 (2011) 215–218, https://doi.org/10.1016/j.cirp.2011.03.112.
[13] D.B. Hann, J. Iammi, J. Folkes, A simple methodology for predicting laser-weld properties from material and laser parameters, J. Phys. D. Appl. Phys. 44 (2011), https://doi.org/10.1088/0022-3727/44/44/445401.
[14] M.C. Sow, T. De Terris, O. Castelnau, Z. Hamouche, F. Coste, R. Fabbro, P. Peyre, Influence of beam diameter on Laser Powder Bed Fusion (L-PBF) process, Addit. Manuf. 36 (2020) 101532, https://doi.org/10.1016/j.addma.2020.101532.
[15] L.R. Goossens, Y. Kinds, J.-P. Kruth, B. Van Hooreweder, On the influence of thermal lensing during selective laser, solid free, Fabr. Symp. – Addit. Manuf. Conf. (2018) 2267–2274, https://www.researchgate.net/publication/329814587.
[16] L. Tatzel, F.P. León, Impact of the thermally induced focus shift on the quality of a laser cutting edge, J. Laser Appl. 32 (2020), https://doi.org/10.2351/7.0000053.
[17] S. Patel, H. Chen, M. Vlasea, Y. Zou, The influence of beam focus during laser powder bed fusion of a high reflectivity aluminium alloy — AlSi10Mg, Addit. Manuf. 59 (2022) 103112, https://doi.org/10.1016/j.addma.2022.103112.
[18] G.E. Bean, D.B. Witkin, T.D. McLouth, D.N. Patel, R.J. Zaldivar, Effect of laser focus shift on surface quality and density of Inconel 718 parts produced via selective laser melting, Addit. Manuf. 22 (2018) 207–215, https://doi.org/10.1016/j.addma.2018.04.024.
[19] A. Paraschiv, G. Matache, M.R. Condruz, T.F. Frigioescu, I. Ionică, The influence of laser defocusing in selective laser melted in 625, Materials 14 (2021) 1–14, https://doi.org/10.3390/ma14133447.
[20] J. Metelkova, Y. Kinds, K. Kempen, C. de Formanoir, A. Witvrouw, B. Van Hooreweder, On the influence of laser defocusing in selective laser melting of 316L, Addit. Manuf. 23 (2018) 161–169, https://doi.org/10.1016/j.addma.2018.08.006.
[21] Y. Yang, Z. Chen, Z. Liu, H. Wang, Y. Zhang, D. Wang, Influence of shielding gas flow consistency on parts quality consistency during large-scale laser powder bed fusion, Opt. Laser Technol. 158 (2023) 108899, https://doi.org/10.1016/j.optlastec.2022.108899.
[22] A. Buades, B. Coll, J.-M. Morel, Non-local means denoising, Image Process. Line 1 (2011) 208–212, https://doi.org/10.5201/ipol.2011.bcm_nlm.
[23] S. Bolte, F.P. Cordelières, A guided tour into subcellular colocalization analysis in light microscopy, J. Microsc. 224 (2006) 213–232, https://doi.org/10.1111/j.1365-2818.2006.01706.x.
[24] NASA, Msfc Technical Standard. Specification for Control and Qualification of Laser Powder Bed Fusion Metallurgical Processes, MSFC-SPEC-3717, 2017.
[25] J. Reijonen, A. Revuelta, H.P.N. Nagarajan, Towards data driven quality monitoring: alignment and correlation of photodiode-based co-axial melt pool monitoring signals to part quality in laser powder bed fusion, IOP Conf. Ser. Mater. Sci. Eng. 1296 (2023) 012009, https://doi.org/10.1088/1757-899X/1296/1/012009.
[26] B. Lane, L. Jacquemetton, M. Piltch, D. Beckett, Thermal calibration of commercial melt pool monitoring sensors on a Laser Powder Bed Fusion System, NIST Adv. Manuf. Ser. 100 (2020) 17, https://doi.org/10.6028/NIST.AMS.100-35.
[27] M. Vänskä, F. Abt, R. Weber, A. Salminen, T. Graf, Effects of welding parameters onto keyhole geometry for partial penetration laser welding, Phys. Procedia 41 (2013) 199–208, https://doi.org/10.1016/j.phpro.2013.03.070.
[28] S.M. Hosseini, E. Vaghefi, E. Mirkoohi, The role of defect structure and residual stress on fatigue failure mechanisms of Ti-6Al-4V manufactured via laser powder bed fusion: Effect of process parameters and geometrical factors, J. Manuf. Process. 102 (2023) 549–563, https://doi.org/10.1016/j.jmapro.2023.07.014.
[29] C. Du, Y. Zhao, J. Jiang, Q. Wang, H. Wang, N. Li, J. Sun, Pore defects in Laser Powder Bed Fusion: formation mechanism, control method, and perspectives, J. Alloy. Compd. 944 (2023) 169215, https://doi.org/10.1016/j.jallcom.2023.169215.
[30] M. Tang, P.C. Pistorius, J.L. Beuth, Prediction of lack-of-fusion porosity for powder bed fusion, Addit. Manuf. 14 (2017) 39–48, https://doi.org/10.1016/j.addma.2016.12.001.
[31] J. Yoshioka, M. Eshraghi, Temporal evolution of temperature gradient and solidification rate in laser powder bed fusion additive manufacturing, Heat. Mass Transf. 59 (2023) 1155–1166, https://doi.org/10.1007/s00231-022-03318-8.
[32] C. Zhao, K. Fezzaa, R.W. Cunningham, H. Wen, F. De Carlo, L. Chen, A.D. Rollett, T. Sun, Real-time monitoring of laser powder bed fusion process using high-speed X-ray imaging and diffraction, Sci. Rep. 7 (1) (2017) 11, https://doi.org/10.1038/s41598-017-03761-2.
[33] Y. Huang, T.G. Fleming, S.J. Clark, S. Marussi, K. Fezzaa, J. Thiyagalingam, C.L. A. Leung, P.D. Lee, Keyhole fluctuation and pore formation mechanisms during laser powder bed fusion additive manufacturing, Nat. Commun. 13 (2022) 1–11, https://doi.org/10.1038/s41467-022-28694-x.
[34] L. Wang, Y. Zhang, H.Y. Chia, W. Yan, Mechanism of keyhole pore formation in metal additive manufacturing, Npj Comput. Mater. 8 (2022), https://doi.org/10.1038/s41524-022-00699-6.
[35] J. Xu, Y. Rong, Y. Huang, P. Wang, C. Wang, Keyhole-induced porosity formation during laser welding, J. Mater. Process. Technol. 252 (2018) 720–727, https://doi.org/10.1016/j.jmatprotec.2017.10.038.
[36] K. Gutknecht, M. Cloots, K. Wegener, Relevance of single channel signals for two-colour pyrometer process monitoring of laser powder bed fusion, Int. J. Mechatron. Manuf. Syst. 14 (2021) 111–127, https://doi.org/10.1504/IJMMS.2021.119152.
[37] A.M. Rubenchik, W.E. King, S.S. Wu, Scaling laws for the additive manufacturing, J. Mater. Process. Technol. 257 (2018) 234–243, https://doi.org/10.1016/j.jmatprotec.2018.02.034.
[38] I. Bitharas, N. Parab, C. Zhao, T. Sun, A.D. Rollett, A.J. Moore, The interplay between vapour, liquid, and solid phases in laser powder bed fusion, Nat. Commun. 13 (2022) 1–12, https://doi.org/10.1038/s41467-022-30667-z.
[39] J.S. Weaver, J.C. Heigel, B.M. Lane, Laser spot size and scaling laws for laser beam additive manufacturing, J. Manuf. Process. 73 (2022) 26–39, https://doi.org/10.1016/j.jmapro.2021.10.053.
[40] W.E. King, H.D. Barth, V.M. Castillo, G.F. Gallegos, J.W. Gibbs, D.E. Hahn, C. Kamath, A.M. Rubenchik, Observation of keyhole-mode laser melting in laser powder-bed fusion additive manufacturing, J. Mater. Process. Technol. 214 (2014) 2915–2925, https://doi.org/10.1016/j.jmatprotec.2014.06.005.
[41] M. Naderi, J. Weaver, D. Deisenroth, N. Iyyer, R. McCauley, On the fidelity of the scaling laws for melt pool depth analysis During Laser Powder Bed Fusion, Integr. Mater. Manuf. Innov. 12 (2023) 11–26, https://doi.org/10.1007/s40192-022-00289-w.
[42] J. Ye, S.A. Khairallah, A.M. Rubenchik, M.F. Crumb, G. Guss, J. Belak, M. J. Matthews, Energy coupling mechanisms and scaling behavior associated with laser powder bed fusion additive manufacturing, Adv. Eng. Mater. 21 (2019), https://doi.org/10.1002/adem.201900185.
[43] R. Fabbro, Scaling laws for the laser welding process in keyhole mode, J. Mater. Process. Technol. 264 (2019) 346–351, https://doi.org/10.1016/j.jmatprotec.2018.09.027.